Mon. Not. R. Astron. Soc. **375,** 931–950 (2007) doi:10.1111/j.1365-2966.2006.11353.x

Radio sources in the 6dFGS: local luminosity functions at 1.4 GHz for star-forming galaxies and radio-loud AGN

Tom Mauch★† and Elaine M. Sadler
School of Physics, University of Sydney, NSW 2006, Australia

Accepted 2006 November 27. Received 2006 November 23; in original form 2006 October 4

ABSTRACT

We have identified 7824 radio sources from the 1.4 GHz NRAO VLA Sky Survey (NVSS) with galaxies brighter than $K = 12.75$ mag in the Second Incremental Data Release of the 6 degree Field Galaxy Survey (6dFGS DR2). The resulting sample of redshifts and optical spectra for radio sources over an effective sky area of 7076 deg^2 (about 17 per cent of the celestial sphere) is the largest of its kind ever obtained. NVSS radio sources associated with galaxies in the 6dFGS span a redshift range $0.003 < z < 0.3$ and have median $\tilde{z} = 0.043$. Through visual examination of 6dF spectra we have identified the dominant mechanism for radio emission from each galaxy. 60 per cent are fuelled by star formation and 40 per cent are fuelled by an active galactic nucleus (AGN) powered by a supermassive black hole. We have accurately determined the local radio luminosity function (RLF) at 1.4 GHz for both classes of radio source and have found it to agree well with other recent determinations. From the RLF of star-forming galaxies we derive a local star formation density of $0.022 \pm 0.001\,\mathrm{M}_\odot\ \mathrm{yr}^{-1}\ \mathrm{Mpc}^{-3}$, in broad agreement with recent determinations at radio and other wavelengths.

We have split the RLF of radio-loud AGNs into bins of absolute K-band magnitude (M_K) and compared this with the underlying K-band galaxy luminosity function of all 6dFGS galaxies to determine the bivariate radio-K-band luminosity function. We verify that radio-loud AGNs preferentially inhabit the brightest and hence most massive host galaxies and show that the fraction of all galaxies which host a radio-loud AGN scales as $f_{\mathrm{radio-loud}} \propto L_K^{2.1}$ for $f_{\mathrm{radio-loud}} < 0.3$, indicative of a similarly strong scaling with black hole mass and stellar mass.

Key words: surveys – galaxies: active – galaxies: luminosity function, mass function – galaxies: starburst – radio continuum: galaxies.

1 INTRODUCTION

In recent years a new generation of radio surveys has been released covering a large fraction of the celestial sphere down to flux density levels of a few mJy [e.g. NRAO VLA Sky Survey (NVSS), Condon et al. 1998; Sydney University Molonglo Sky Survey (SUMSS), Bock, Large & Sadler 1999 and Mauch et al. 2003; Faint Images of the Radio Sky at Twenty-cm (FIRST), Becker, White & Helfand 1995; Westerbork Northern Sky Survey (WENSS), Rengelink 1998]. The vast majority of the radio sources in these surveys are produced by active galactic nuclei (AGNs) powered by supermassive black holes in galaxies with a median redshift of $z \approx 0.8$ (Condon et al. 1998). These dominate the radio source population above flux densities of 10 mJy. Below 10 mJy the surveys contain an increasing fraction of nearby ($z < 0.1$) galaxies whose radio emission is fuelled by ongoing star formation (Condon 1989). Because radio surveys probe a wide range of redshifts, studying their global properties statistically (e.g. through radio source counts or luminosity functions) provides a powerful constraint on the evolutionary properties of massive galaxies throughout the history of the Universe. Unfortunately, radio survey data alone are not sufficient to constrain the current models of radio source counts. These models are strongly dependent on the form of the *local* radio luminosity function (RLF) from which the measured source counts can be extrapolated via evolutionary models (e.g. Dunlop & Peacock 1990; Jackson & Wall 1999) or compared directly to the measured RLF of samples selected at higher redshift (e.g. Brown, Webster & Boyle 2001; Sadler et al. 2006). The current generation of redshift surveys [e.g. Sloan Digital Sky Survey (SDSS), York et al. 2000; 2 degree Field Galaxy Redshift Survey (2dFGRS), Colless et al. 2001; 6 degree Field Galaxy Survey (6dFGS), Jones et al. 2004] provide a useful tool for calculating the local RLF, as they provide redshifts for thousands of radio sources in the local Universe. The

★E-mail: txm@astro.ox.ac.uk
†Present address: Astrophysics, Department of Physics, Denys Wilkinson Building, University of Oxford, Keble Road, Oxford OX1 3RH.

Table 1. Comparison of recent radio-selected samples used to derive the local RLF.

	UGC–NVSS Condon et al. (2002)	6dFGS–NVSS This paper	2dFGRS–NVSS Sadler et al. (2002)	2dFGRS–FIRST Magliocchetti et al. (2002)	SDSS–NVSS/FIRST Best et al. (2005b)
			SF galaxies		
No. of galaxies	1672	4006	242	177	497
Magnitude limit	$m_{\rm p} < 14.5$	$K_{\rm tot} < 12.75$	$14.0 \leqslant b_J \leqslant 19.4$	$14.0 \leqslant b_J \leqslant 19.45$	$14.5 < r < 17.77$
$S_{\rm lim}$ (mJy)	2.5	2.8	2.8	1.0	5.0
Area(sr)[a]	4.33	2.16	0.10	0.07	$\sim$0.4[e]
z range[b]	$\lesssim$0.04	$\lesssim$0.1	$\lesssim$0.15	$\lesssim$0.25	$\lesssim$0.15
Median z	0.012	0.035	0.043	0.100	0.055
Volume (10^6 Mpc^3)[c]	7	53	8	22	$\sim$30[e]
τ (Gyr)[d]	0.543	1.30	1.89	2.94	1.89
$\rho_{\rm SF}$ M$_\odot$ yr^{-1} Mpc^{-3}	0.018	0.022	0.031		
			Radio-loud AGNs		
No. of galaxies	294	2661	420	372	2215
Magnitude limit	$m_{\rm p} < 14.5$	$K_{\rm tot} < 12.75$	$14.0 \leqslant b_J \leqslant 19.4$	$14.0 \leqslant b_J \leqslant 19.45$	$14.5 < r < 17.77$
$S_{\rm lim}$ (mJy)	2.5	2.8	2.8	1.0	5.0
Area(sr)[a]	4.33	2.16	0.10	0.07	$\sim$0.4[e]
z range[b]	$\lesssim$0.04	$\lesssim$0.2	$\lesssim$0.3	$\lesssim$0.3	$\lesssim$0.3
Median z	0.019	0.073	0.140	0.150	0.165
Volume (10^6 Mpc^3)[c]	7	391	58	40	$\sim$230[e]
τ (Gyr)[d]	0.543	2.44	3.44	3.44	3.44

[a]For the 2dFGRS–NVSS and 6dFGS–NVSS samples the area is the effective area as defined in Section 2.3.
[b]The maximum redshift of each survey has been estimated from the redshift histogram.
[c]Volumes are calculated to the maximum redshift of each survey and reduced by the fraction of sky surveyed.
[d]τ is the look-back time in Gyr and is calculated from the maximum redshift of each survey.
[e]As Best et al. (2005b) did not calculate the sky area of the SDSS–NVSS/FIRST sample, we have roughly estimated it from coverage plots.

host galaxy spectra provide additional value in this context as they can be used to determine the physical cause of the radio emission from galaxies, thereby disentangling the star-forming (SF) galaxy population from the radio-loud AGNs.

Table 1 compares the underlying radio-optical samples used in recent measurements of the local RLF. Sadler et al. (2002) identified NVSS radio sources in the 2dFGRS and derived the local RLF of both SF galaxies and radio-loud AGNs; this will hereafter be referred to as the 2dFGRS–NVSS sample. Magliocchetti et al. (2002) identified optical counterparts to FIRST galaxies in the 2dFGRS; this will hereafter be referred to as the 2dFGRS–FIRST sample. Both the radio-selected 2dFGRS samples cover a relatively small area of sky to redshifts of $z \approx 0.3$ and predominantly comprise radio-loud AGNs. In particular the 2dFGRS–FIRST sample detected relatively few SF galaxies as the high-resolution FIRST survey resolves out much of the extended radio emission in the disks of nearby galaxies. Best et al. (2005b) identified NVSS and FIRST radio sources in the second data release of the SDSS; this will hereafter be referred to as the SDSS–NVSS/FIRST sample. They optimized their radio-source selection via a hybrid method which used both the resolution of the FIRST survey and the surface brightness sensitivity of the NVSS survey. However, they detected relatively few SF galaxies above their adopted flux density limit of 5 mJy. Condon, Cotton & Broderick (2002) cross-matched the NVSS catalogue with galaxies brighter than $m_{\rm p} = 14.5$ mag in the Uppsala Galaxy Catalogue (UGC; Nilson 1973) and constructed a sample of 1966 radio sources in the local ($z < 0.03$) Universe across 4.33 sr of the northern sky; this will hereafter be referred to as the UGC–NVSS sample. The wide yet shallow UGC–NVSS sample contained a large population of SF galaxies but relatively few radio-loud AGNs. Larger numbers of radio-loud AGNs are found at higher redshifts.

This paper presents the local RLF derived from a well-defined subsample of the 7824 radio sources from the NVSS catalogue identified with galaxies observed in the Second Incremental Data Release (DR2) of the 6dFGS; this will be referred to as the 6dFGS–NVSS sample. Galaxies in the 6dFGS–NVSS sample presented in this paper lie at redshifts intermediate between the more distant 2dFGRS–NVSS and SDSS–NVSS/FIRST samples and the nearby UGC–NVSS sample, in an effective sky area much larger than that of the 2dFGRS and SDSS derived samples. 6dFGS–NVSS galaxies are contained in a larger volume of space than any previous local radio source sample, with significant populations of both radio-loud AGNs and SF galaxies all contained in the one survey.

The RLF derived in this paper has a number of advantages over previous determinations:

(i) The near-infrared (NIR) and radio input catalogues are from homogeneous surveys with a single instrument, and avoids biases which may result from combining surveys.

(ii) The digital K-band magnitudes from the 2MASS XSC are more accurate than those which have been derived from measurements of photographic plates (e.g. 2dFGRS, UGC).

(iii) The NIR selection of the 6dFGS means it is relatively unaffected by dust in both the target galaxy and our own Galaxy. This means that the radio selected sample will not be biased with respect to the amount of dust in the host galaxy, which can steer surveys away from galaxies with higher star formation rates. NIR magnitudes are also more closely linked to the old stellar population in galaxies, effectively tipping the balance in favour of massive early-type galaxies which preferentially host radio-loud AGNs.

(iv) The large sample volume of the 6dFGS contains more radio sources than any previous radio-selected galaxy sample (see Table 1).

The structure of this paper is as follows. Section 2 describes the 6dFGS and NVSS surveys and our method of identifying radio sources in the 6dFGS. Section 3 outlines the global properties of 6dFGS–NVSS galaxies. Section 4 examines the population of primary sample objects which are detected in the *Infrared Astronomical Satellite* (*IRAS*) Faint Source Catalogue (FSC) (*IRAS*–FSC), both as a consistency check for the spectroscopic classification of the sample and to derive the radio–far-infrared (radio–FIR) correlation for a larger sample of SF galaxies than any obtained to date. Section 5 presents the local RLF at 1.4 GHz for the radio-loud AGNs and SF galaxies. Section 6 presents a derivation of the star formation density at the present epoch. Section 7 presents the bivariate radio–NIR luminosity function of radio-loud AGNs. Finally, Section 8 summarizes the main results. Throughout, if not explicitly stated, we adopt a ΛCDM cosmology with parameters $\Omega_{\rm m} = 0.3, \Omega_\Lambda = 0.7$ and $H_0 = 70\,{\rm km\,s^{-1}\,Mpc^{-1}}$ (Spergel et al. 2003).

2 SAMPLE SELECTION

2.1 The 6 degree Field Galaxy Survey

The 6dFGS is a spectroscopic survey of about 170 000 objects in the 17 046 deg^2 of sky with declination $\delta < 0^\circ$ and galactic latitude $|b| > 10^\circ$. The survey was carried out on the 1.2 m UK Schmidt Telescope at Siding Spring Observatory. The majority of targets (113 988) are NIR selected to be complete to an apparent magnitude limit of $K = 12.75$ mag from the Two Micron All-Sky Survey Extended Source Catalogue (2MASS XSC; Jarrett et al. 2000) and comprise the 6dFGS *primary sample*. The remainder of the survey is filled out by a number of smaller additional target samples selected in various ways at other wavelengths (Jones et al. 2004). The spectroscopic sample considered in this paper consists of the 47 317 objects from the *K*-selected primary sample that have been observed during the period 2002 January to 2004 October and released in the DR2 (Jones et al. 2005) of the 6dFGS and that overlap with southern part of the NVSS survey ($-40^\circ < \delta < 0^\circ$).

6dFGS spectra are obtained through 6 arcsec diameter fibre buttons which correspond to a projected diameter of 6.8 kpc at the median redshift of the survey ($\tilde{z} \sim 0.05$). 6dF fibres include an increasing fraction of total galaxy light for higher redshift galaxies, and therefore galaxies with emission-line nuclei are easier to recognize at lower redshift. 6dFGS observations prior to 2002 October were made with reflection gratings and cover a wavelength range of 4000–8400 Å. Since 2002 October observations were made with volume-phase transmissive holographic (VPH) gratings, which have provided improved efficiency and data uniformity and cover a wavelength range of 3900–7500 Å. Primary target spectra typically have resolution $R \sim 1000$ and signal-to-noise ratio (S/N) of $10\,{\rm pixel^{-1}}$ allowing redshifts and host galaxy parameters (i.e. emission-line ratios) to be readily determined. Redshifts are measured from the spectra using the RUNZ package described by Jones et al. (2004) and assigned a quality class Q by human operators based on the reliability of the measured redshift. Only $Q = 3$ or 4 redshifts are expected to be reliable, $Q = 6$ redshifts are reserved for Galactic sources (see Jones et al. 2005, for a complete description).

The total *K*-band magnitudes ($K_{\rm tot}$) used for selection of 6dFGS primary targets have been derived from isophotal magnitudes ($K_{\rm iso}$) and diameters to an elliptical isophote of $\mu_K = 20\,{\rm mag\,arcsec^{-2}}$ (equation 1 of Jones et al. 2004). These *derived* values of $K_{\rm tot}$ are more robust than those quoted in the 2MASS XSC and have therefore been used throughout this paper. The derived *K* magnitudes have typical errors $\Delta K < 0.1$ mag and the NIR-selected sample is complete to the survey limit of $K = 12.75$ mag (Jones et al. 2006).

2.2 The NRAO VLA Sky Survey

The NVSS is a 1.4 GHz imaging survey of the entire sky north of $\delta = -40^\circ$ carried out on the Very Large Array (VLA) telescope in its DnC and D configurations. Its principal data products are a set of 2326 4×4 deg^2 continuum images and a catalogue of about 2×10^6 fits of elliptical Gaussians to discrete sources stronger than $S_{1.4\,{\rm GHz}} \approx 2$ mJy. The images have $\theta = 45$ arcsec FWHM resolution with position accuracy $\leqslant$1 arcsec for sources stronger than 15 mJy, increasing to >7 arcsec at the survey limit (Condon et al. 1998). The resolution and positional accuracy of the NVSS makes identification of radio sources with objects on optical survey plates straightforward in the majority of cases. There are 580 419 NVSS catalogue sources which overlap with the 6dFGS; a region bounded by $0^\circ > \delta > -40^\circ$, $|b| > 10^\circ$. These sources form the primary 1.4 GHz-selected input catalogue for the 6dFGS–NVSS sample.

2.3 Sky coverage

The 6dFGS uses a tiling algorithm with variable overlap depending on the underlying galaxy density (Campbell, Saunders & Colless 2004). Because of this and because not all 6dFGS tiles were observed in the DR2 (Jones et al. 2005), calculating the exact area of sky surveyed is not straightforward. A method of calculating sky area for surveys with gaps in coverage such as the 6dFGS DR2 was described by Folkes (1999) and was also applied to 2dFGRS–NVSS galaxies by Sadler et al. (2002). This method estimates the area of sky covered by dividing the number of galaxies observed by the mean surface density of galaxies in the survey target list. The surface density of 6dFGS primary targets is 6.7 objects deg^{-2}. 47 317 primary targets north of -40° have been observed in the DR2. Therefore the effective area is 7076 deg^2, or 17.15 per cent of the celestial sphere. Calculation of the effective area in this way also accounts for the 5 per cent fibring incompleteness of the 6dFGS. However, it takes no account of the small amount of incompleteness due to failed observations (e.g. low-S/N spectra); this is discussed in more detail in Section 5.

2.4 Cross-matching the 6dFGS primary sample with the NVSS

When searching for NVSS radio source identifications of the 6dFGS primary targets we used a method which aimed to maximize both the completeness (i.e. all potential radio sources are included) and the reliability (i.e. all included radio identifications are genuine) of the data base. To ensure a high completeness and reliability of NVSS–2MASS identifications we determine a maximum position offset which includes all possible identifications, construct a list of these identifications and then verify each of them by visually inspecting overlays of radio contours on to optical images. Although checking all identifications by eye is time consuming, in our experience it is the best way to minimize the number of false identifications, as at all separations some radio identifications selected by position offset alone will be chance coincidences. Visual inspection of every radio-optical overlay also allows us to correct the catalogued flux densities of confused or diffuse sources for which the elliptical Gaussian model used in the NVSS catalogue does not measure reliable radio source parameters. Our visual identification method closely follows that described by both Condon et al. (2002)

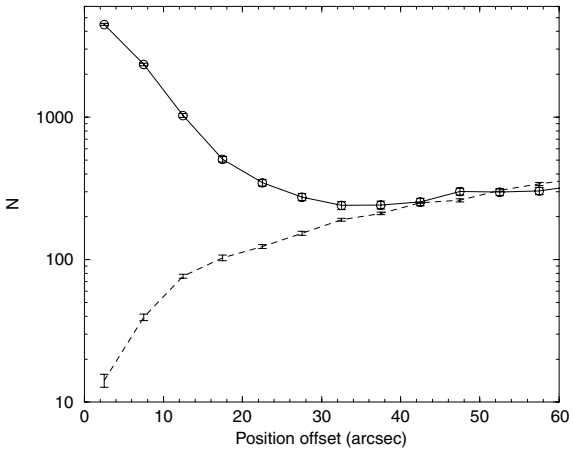

Figure 1. For all 25 096 6dFGS primary targets with a single NVSS catalogue source within 3 arcmin, the open circles linked by a solid line show the distribution of position offsets to the radio source. The dashed line shows the average distribution of position offsets to NVSS catalogue sources from positions in five random catalogues with the same size and sky coverage as the 6dFGS primary sample, also with a single radio source within 3 arcmin.

and Sadler et al. (2002); the reader is referred to those papers for examples and descriptions of radio source identifications with bright galaxies in optical images.

To include all possible radio source identifications, we decided to consider all radio sources with NVSS–2MASS position offset less than 3 arcmin. This offset was chosen as it is large enough to include the majority of possible multicomponent radio galaxies while still smaller than the average separation of unrelated radio sources in the NVSS catalogue. Of the 74 609 6dFGS primary sample targets north of -40°, 34 097 of them had at least one identification in the NVSS catalogue within 3 arcmin, of which 21 597 were observed in the 6dFGS DR2. We chose to examine the 15 716 6dFGS DR2 galaxies that have a single NVSS identification within 3 arcmin separately from the 5881 with more than one.

2.4.1 Single-component radio sources

For all 25 096 6dFGS primary targets with a single NVSS catalogue match within 3 arcmin, the solid line in Fig. 1 shows the distribution of position offsets of radio sources from the 6dFGS galaxy (in arcsec). Five random catalogues containing 74 609 positions (the same as the number of all 6dFGS primary targets) and covering the same region of sky as the 6dFGS–NVSS sample were also matched with the NVSS catalogue. For the random positions with only a single NVSS match within 3 arcmin, the average of the five resulting distributions of NVSS–2MASS position offsets is shown as a dashed line in Fig. 1. At 40 arcsec the expected number of random matches is the same as the number of real matches so we conclude that all single-component NVSS matches with 6dFGS primary targets that have position offset >40 arcsec are not genuine.

5829 6dFGS DR2 primary targets with a single NVSS catalogue match within 3 arcmin have position offset <40 arcsec. The dashed line in Fig. 1 implies that at separations <40 arcsec some misassociations are expected. We visually inspected overlays of NVSS radio contours on to b_J images from the SuperCOSMOS Sky Survey (Hambly et al. 2001) for each candidate identification and classified them as follows:

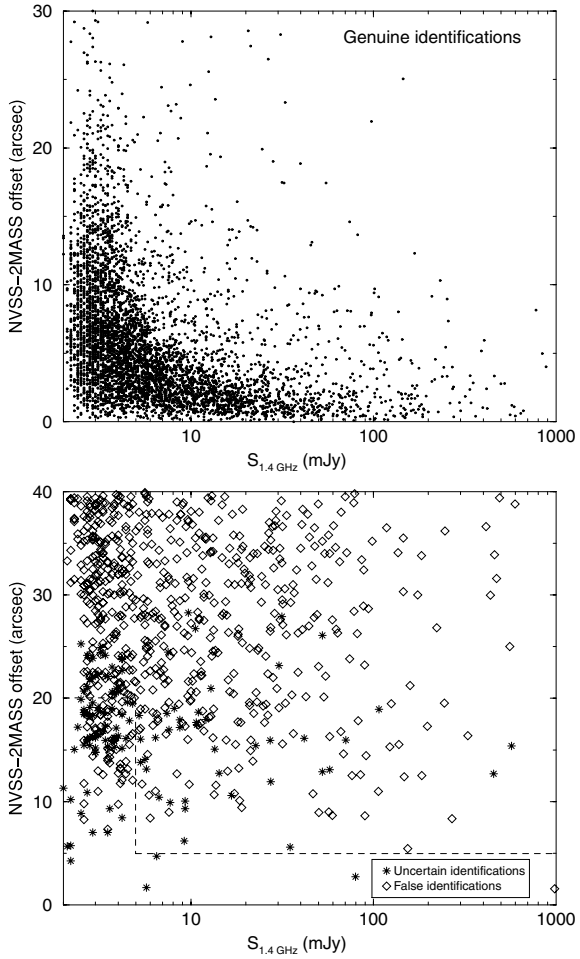

Figure 2. The results of visual identification of 5829 6dFGS DR2 primary sample objects with a single NVSS catalogue match within 3 arcmin. The top figure shows the 5016 real identifications, we found no genuine identifications with NVSS–2MASS offset >30 arcsec. In the bottom figure, diamonds show the 693 false identifications and stars show the 120 uncertain identifications. The dashed line shows the adopted cut-off used to accept uncertain identifications.

(i) *Genuine* (5016 candidates), for objects whose radio-optical identification is unambiguously real.

(ii) *False* (693 candidates), for objects whose radio-optical identification is unambiguously not real. This is usually because the radio source is identified with another galaxy on the optical image.

(iii) *Uncertain* (120 candidates), for objects whose radio optical identification is ambiguous. This is usually because two possible host galaxies can be seen within the NVSS position error ellipse.

Fig. 2 shows our hand classification of 6dFGS–NVSS candidates. We find no genuine identifications of single-component radio sources with position offset between 30 and 40 arcsec. The excess of real over random identifications of NVSS radio sources at these separations seen in Fig. 1 is likely to have been caused by the clustering of galaxies as was noted by Best et al. (2005b); at a real galaxy position, there is more likely to be a companion which is the true radio source identification within 100 arcsec than at a random position on the sky. For accepted NVSS–2MASS identifications the increasing range of position offsets with decreasing NVSS flux density reflects the increase in position uncertainties for fainter radio sources

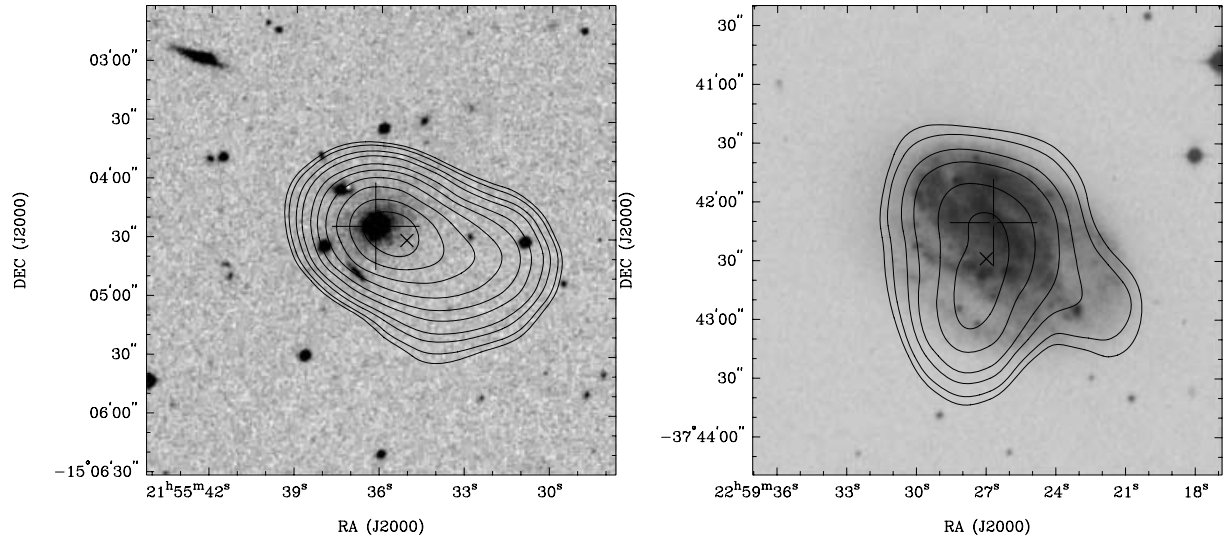

Figure 3. Radio contours from the NVSS overlaid on to b_J images from the SuperCOSMOS Sky Survey for two accepted 6dFGS–NVSS identifications with fitted positions in the NVSS catalogue more than 15 arcsec from galaxy positions in the 2MASS XSC. In both images cross-hairs show the 2MASS XSC galaxy position and a small cross labels the fitted position of the radio source in the NVSS catalogue. The contour levels plotted in both images are: 2.5, 3, 4, 5, 7, 9, 12, 16, 21, 26 and 30 mJy beam^{-1}. The left-hand image shows the 6dFGS galaxy g2155362−150424 at $z = 0.07$. The catalogued $S_{1.4\,\mathrm{GHz}} = 55$ mJy NVSS radio source is 17.5 arcsec from the host galaxy position. Its Aa spectrum (as defined in Table 2) implies that this is a radio-loud AGN and all of the extended radio emission is associated with the host galaxy. The right-hand image shows the 6dFGS SF galaxy g2259267−374210 at $z = 0.004$. The catalogued $S_{1.4\,\mathrm{GHz}} =$ 39.8 mJy NVSS radio source is 18.9 arcsec from the host galaxy position. This source has a complex radio structure and we have therefore corrected its 1.4 GHz flux density to 42.5 mJy by adding up the pixels in the radio image.

(Condon et al. 1998). It is clear that there is no simple NVSS–2MASS offset cut-off which separates real identifications from false identifications. The vast majority of real identifications have small (i.e. <15 arcsec) position offsets though there is still about 2 per cent contamination by false identifications with smaller separations at all NVSS flux densities. Conversely, some real identifications are found with offset >15 arcsec. This is due to a number of factors:

(i) Complex and asymmetric radio sources can have fitted positions in the NVSS catalogue which differ by more than 15 arcsec from the galaxy positions in the 2MASS XSC. Two examples are shown in Fig. 3.

(ii) Some galaxies can appear at the position of one of the lobes of a double radio source whose centroid is associated with another galaxy. This can lead to false identifications of radio sources with offsets <15 arcsec.

(iii) One of a pair of galaxies with small separation can be identified with a radio source which is clearly identified with the other galaxy. This can lead to false identifications of radio sources with offsets <15 arcsec.

We found 120 candidate identifications which had two or more optical galaxies visible on SuperCOSMOS b_J images inside the 3σ NVSS position error ellipse (shown as stars in Fig. 2). These candidates were considered too uncertain to make a definitive visual classification. We chose to accept as a genuine match the 55 objects with position offset <20 arcsec for radio sources with $S_{1.4\,\mathrm{GHz}} \leqslant 5$ mJy and position offset <5 arcsec for radio sources with $S_{1.4\,\mathrm{GHz}} > 5$ mJy. This cut-off is shown as a dashed line in Fig. 2. In the region of the figure below this line more than 99 per cent of unambiguous identifications (i.e. both genuine and false) are genuine, so we expect that less than 1 per cent of unsure identifications will be misidentified by applying the cut-off.

2.4.2 *Multiple-component radio sources*

A further 5881 6dFGS DR2 galaxies had more than one identification in the NVSS catalogue within 3 arcmin. We chose to examine all such candidates by visual examination of SuperCOSMOS b_J images overlaid with NVSS contours. In 3226 of them, one of the radio components lay within 40 arcsec of the galaxy. These were either the cores of multiple-component radio sources or a single-component radio source and other unrelated NVSS radio sources within 3 arcmin. We chose to accept or reject such candidates using the method outlined in Section 2.4.1 for single-component radio sources and accepted further 2716 radio source identifications. We determined NVSS flux densities for accepted multiple-component radio sources by summing the individual catalogued flux densities of each component.

We visually classified the remaining 2655 candidate multiple-component radio sources which have no NVSS catalogue match within 40 arcsec of the host galaxy. Classification of such objects by eye is straightforward as the sensitivity of the NVSS to extended radio emission makes it easy to identify large connected structures in the radio images. For brighter radio sources, we supplemented our visual classification by double-checking our identifications with previous optical identifications of radio sources from the Revised Third Cambridge catalogue of radio sources (3CR; Laing, Riley & Longair 1983), the Parkes–MIT–NRAO survey catalogue (PMN; Griffith & Wright 1993) and the Molonglo Reference Catalogue of radio sources (MRC; Large et al. 1981). A further 37 multiple-component radio sources were identified out of the 2655 candidates.

2.4.3 *Giant radio galaxies*

A detection of at least one NVSS radio component within 3 arcmin of the host galaxy is required to identify a radio source using our identification procedure. This implies that we miss any population

of giant radio galaxies (GRGs) (Schoenmakers et al. 2001; Saripalli et al. 2005) which have linear sizes in excess of 6 arcmin in radio images and no detection of a core. About half of the GRGs in a sample selected by Saripalli et al. (2005) have lobes that are detected at the limit of the SUMSS catalogue but cores that are not. The space density of GRGs with linear size greater than 5 arcmin measured by Saripalli et al. (2005) is 10^{-7} Mpc^{-3} for $z < 0.4$, which implies that about 40 such GRGs would be found in the 6dFGS–NVSS sample volume. About 1/3 of these would be missed by our identification procedure (i.e. those with linear size >6 arcmin and no detection of a core). GRGs are powerful radio sources and have typical 1.4 GHz radio powers between $10^{23.5}$ and 10^{26} W Hz^{-1}. We expect that the incompleteness of the 6dFGS–NVSS sample in this radio power range will be no greater than 1 per cent because of missing GRGs.

2.4.4 Reliability and completeness

It is possible to estimate the reliability and completeness of the data base for single-component radio sources using the data presented in Fig. 1. We expect our visual classification scheme to be most robust for identifications of radio sources within 15 arcsec of the host galaxy position. Integrating under the dashed line in Fig. 1 out to 15 arcsec and scaling to the number of objects observed implies that 81 random associations with radio sources are expected. During visual classification we rejected 74 candidate matches and therefore an estimated seven accepted identifications in this region are spurious. The remainder of the accepted matches had offsets between 15 arcsec and 30 arcsec. We expect 238 random associations with offsets in this region and during visual identification rejected 361 candidate matches. This implies that 123 genuine identifications in this region have been spuriously classified as false. We believe that the majority of these spuriously rejected identifications have been made for fainter ($S_{1.4\,\mathrm{GHz}} < 2.8$ mJy) radio sources many of whose NVSS position errors exceed 10 arcsec. Finally, we accepted no radio source identifications with position offset between 30 and 40 arcsec, however based on the small excess of real over random matches seen in this region of Fig. 1 we expect there to be 51 genuine associations. This means that for single-component radio sources in the final data base, 7/5016 accepted matches are spurious, corresponding to a reliability of close to 100 per cent, and (123 + 51) = 174 matches have been erroneously rejected, corresponding to a completeness of 97 per cent. Our estimate of completeness is likely to be a lower limit because many of the excess real over random matches at separations greater than 15 arcsec are associated with galaxy pairs as was noted in Section 2.4.1. The reliability and completeness of the 2716 identifications with more than one NVSS catalogue identification within 3 arcmin and a radio component within 40 arcsec of the host galaxy mimics that of the single-component radio sources.

The reliability and completeness of multiple-component radio source identifications with no NVSS detection with 40 arcsec of the host galaxy is difficult to determine. For the brightest sources, we cross-matched the 6dFGS–NVSS data base with well-studied data bases of optical identifications from the 3CR, PMN and MRC data bases and found no spurious or missing identifications which implies our completeness and reliability are 100 per cent. We assume this extends to fainter radio source identifications in the 6dFGS–NVSS sample. Multiple-component radio source identifications are rare (they comprise <1 per cent of all radio sources in this sample) and we believe these cannot affect the completeness and reliability in a significant way. The missing population of GRGs described in Section 2.4.3 also contributes <1 per cent to the incompleteness of 6dFGS–NVSS identifications.

In summary, we find that the completeness of the 6dFGS–NVSS data base is better than 96 per cent (a 3 per cent contribution from missing single-component matches and a ∼1 per cent contribution from missing multiple-component matches). The reliability of the data base is better than 99 per cent. Recently, Best et al. (2005b) described a robust identification method utilizing both the FIRST and NVSS surveys to find radio sources in the SDSS and their matching procedure had an estimated completeness of 94.4 per cent and reliability of 98.9 per cent. The FIRST survey only covers about 1 per cent of the region observed in the 6dFGS DR2 and we were therefore unable to use their method. We achieve similar (or slightly better) completeness and reliability to them by visually classifying all radio-optical identifications; we believe this is the most robust method of identifying radio sources in optical sky surveys when only the NVSS is available.

2.5 Classification of 6dFGS optical spectra

The 6dF spectrum of each accepted radio source identification was inspected visually to determine the dominant physical process responsible for the radio emission of each galaxy. We followed the scheme described by Sadler et al. (2002) and classified each spectrum as either 'AGNs' for spectra indicative of galaxies harbouring a radio-loud AGN or 'SF' for spectra indicative of galaxies with ongoing star formation. AGNs can have a pure absorption-line spectrum like that of a giant elliptical galaxy (classed as Aa); a spectrum with absorption lines and weak narrow LINER-like emission lines (classed as Aae); a conventional Type II AGN spectrum which has nebular emission lines such as [O II], [O III] or [N II] which are stronger than any hydrogen Balmer emission lines (Hα or Hβ) (classed as Ae); or a conventional Type I AGN spectrum with strong and broad hydrogen Balmer emission lines (also classed as Ae). SF galaxies have spectra typical of H II regions with strong narrow emission lines of Hα and Hβ dominating the spectrum (classed as SF). Fig. 4 shows an example of each type of spectrum. Spectra of galactic stars were classified 'star' and spectra for which a classification could not be made (mostly due to a low-S/N spectrum) were classed '?'. A '?' was also appended to the end of any classification which was not certain. Our visual classification scheme is summarized in Table 2.

To check the reliability of the visual classification scheme a subsample of ∼1800 spectra was classified by both of us and the classifications compared. The two human classifiers agreed well, with disagreement in about 10 per cent of cases. The primary cause of disagreement is between the classification of emission-line AGNs (Aae and Ae classes) and the SF class, and occurs for spectra which have line ratios which are borderline between the AGN and SF classes. If only the AGN and SF classes are considered then the two human classifiers disagree only 5 per cent of the time. In their analysis of 2dFGS spectra using the same classification scheme described here, Sadler et al. (2002) found that this scheme agreed well with methods such as principal component analysis (PCA; Folkes 1999; Madgwick et al. 2002) and classification based upon diagnostic emission-line ratios (Jackson & Londish 2000) both of which have a similar reliability to that of the visual classification presented here.

3 SAMPLE PROPERTIES

We matched a total of 7824 6dFGS DR2 primary targets with radio sources from the NVSS catalogue, corresponding to a radio

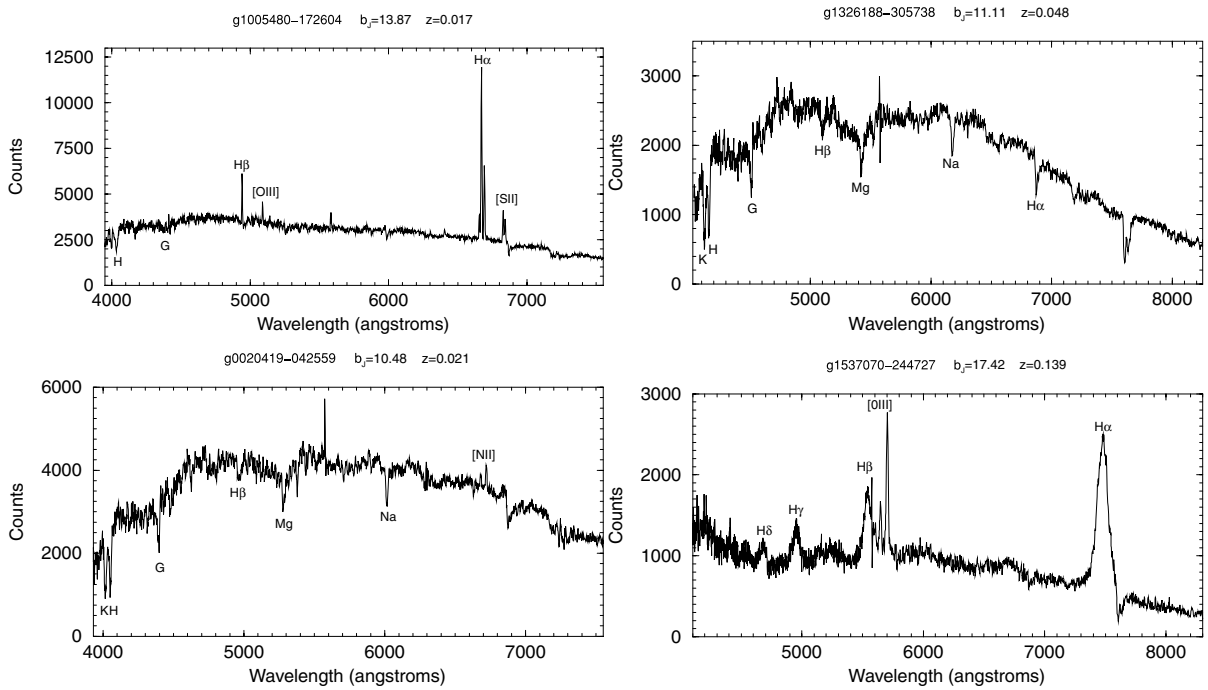

Figure 4. Example 6dFGS spectra of four spectral classes. In each spectrum common redshifted absorption/emission lines are labelled at the measured redshift. Top left-hand panel: An 'SF' galaxy, with characteristic strong and narrow Balmer lines. Top right-hand panel: An 'Aa' galaxy, containing broad Mg absorption as well as a distinct break close to the H & K lines. Bottom left-hand panel: An 'Aae' galaxy. This looks similar to an 'Aa' galaxy but has a weak [N II] line. Bottom right-hand panel: An 'Ae' galaxy. This has broad Hα emission and strong [O III] lines.

Table 2. Spectral classes visually assigned to 6dFGS–NVSS objects.

Class	Type of spectrum	Number
Aa	Pure absorption-line spectrum	2124
Aae	Narrow LINER-like emission lines	370
Ae	Emission line AGNs	370
SF	SF galaxy	4625
?	Unclassifiable or unknown	321
Star	Galactic star	14
Total		7824

detection rate of 16.5 per cent. Of the 7824 detections, 7672 were identified with a single NVSS component and 152 were identified with more than one. Table 2 summarizes the spectral properties of the accepted 6dFGS–NVSS matches. Out of the 7824 spectra we examined, 321 were unclassifiable (classed as '?') and 14 of them were Galactic stars (assigned redshift quality $Q = 6$ in the 6dFGS). Of the unclassifiable spectra, 302 had redshift quality $Q = 1$ or 2, these spectra were too noisy for reliable spectral classification. The remaining 19 unclassifiable spectra had reliable redshift measurements, but did not present enough information for reliable visual classification.

The ratio of SF galaxies to radio-loud AGNs in the sample is approximately 60 per cent SF to 40 per cent radio-loud AGNs. The fractions of SF to radio-loud AGNs in the similarly classified 2dFGRS–NVSS sample (Sadler et al. 2002) are 40 per cent SF to 60 per cent radio-loud AGNs. The difference in these relative fractions can be explained by the fainter magnitude limit ($b_J = 19.4$) of the 2dFGRS, resulting in a larger proportion of detections of more distant radio-loud AGNs. It is interesting that in both the 6dFGS–NVSS and 2dFGRS–NVSS samples, over 70 per cent of all radio-loud AGNs have absorption-line spectra and would be missed from AGN samples selected on the basis of optical emission lines.

3.1 The data table

Table 3 shows details of the sample of 6dFGS–NVSS radio sources. The 6dFGS target name is given for each source so that the observed 6dFGS spectra can be obtained or each object can be matched against other 6dFGS additional target samples (Jones et al. 2004). The table also shows 2MASS XSC J2000 positions, derived $K_{\rm tot}$, redshifts and redshift quality Q for each source. We list offsets from the given position and integrated 1.4 GHz flux densities for each NVSS radio source. For single-component NVSS radio sources with an 843 MHz SUMSS catalogue (version 1.6) detection within 10 arcsec we also list the 843 MHz flux density of the source. The list of SUMSS matches is highly incomplete at present as the 6dFGS DR2 covers little of the sky south of $\delta = -40^\circ$ and version 1.6 of the SUMSS catalogue is not complete north of this declination. We plan to thoroughly investigate the properties of SUMSS radio sources in the 6dFGS when the full data releases of both surveys are made available and this will be the subject of a future paper. For objects with a match in the 6dFGS additional target sample selected from the *IRAS*–FSC (Moshir et al. 1993) (programme ID 126; Jones et al. 2004) we list the 60 μm flux density of the source. The final column of the table shows the visually assigned spectral classification described in Section 2.5.

3.2 Radio source counts

The differential source counts of 6dFGS–NVSS galaxies are plotted in Fig. 5. These are plotted in a form in which each bin is weighted

Table 3. The first 30 entries of the 6dFGS–NVSS data table.

(1) 6dFGS target name	(2) RA (J2000) ($^h:^m:^s$)	(3) Dec. (J2000) ($^\circ:':''$)	(4) K (mag)	(5) z	(6) Q	(7) Offset (arcsec)	(8) $S_{1.4\,GHz}$ NVSS (mJy)	(9) $S_{843\,MHz}$ SUMSS (mJy)	(10) $S_{60\,\mu m}$ *IRAS*–FSC (Jy)	(11) Spectrum class
g0000124−363113	00:00:12.39	−36:31:13.1	12.724	0.1169	4	9.5	12.1			Aa
g0000141−251113	00:00:14.12	−25:11:12.9	11.886	0.0852	4	3.8	28.4			Aa
g0000356−014547	00:00:35.64	−01:45:47.4	11.267	0.0246	4	15.4	2.8			Aae?
g0000523−355037	00:00:52.33	−35:50:37.2	11.330	0.0521	4	0.0	48.4			Aa
g0001197−140423	00:01:19.74	−14:04:23.2	12.289	0.0867	3	11.0	40.5			Aae?
g0001394−025852	00:01:39.36	−02:58:52.1	12.001	0.1013	4	2.3	5.5			Aa
g0001453−042049	00:01:45.29	−04:20:49.0	11.845	0.0481	4	5.0	2.8			Aa
g0001496−094138	00:01:49.58	−09:41:37.8	12.304	0.1038	4	13.8	3.4			Aa
g0001558−273738	00:01:55.82	−27:37:38.0	10.164	0.0283	4	4.3	29.8		0.488	SF
g0001567−035755	00:01:56.70	−03:57:54.8	12.492	0.0226	4	2.3	6.2		0.466	SF
g0001572−383857	00:01:57.20	−38:38:56.4	12.644	0.0547	4	2.5	11.8	22.9		SF
g0002039−332802	00:02:03.88	−33:28:02.2	11.143	0.0289	4	4.2	6.2		0.941	SF
g0002348−034239	00:02:34.81	−03:42:38.6	10.623	0.0215	4	0.3	13.1		1.121	SF
g0002487−033622	00:02:48.65	−03:36:21.7	11.455	0.0208	4	6.9	3.9			SF
g0002547−354319	00:02:54.69	−35:43:19.4	11.677	0.0489	4	24.0	4.2			Aa
g0002545−341408	00:02:54.47	−34:14:08.4	10.699	0.0226	4	2.6	7.3		0.760	SF
g0002558−265451	00:02:55.81	−26:54:51.2	11.994	0.0665	4	1.1	94.4			Aa
g0003051−073700	00:03:05.06	−07:37:00.3	12.291	0.0299	4	6.3	3.7			Aae
g0003057−015450	00:03:05.66	−01:54:49.7	10.156	0.0244	4	1.1	7.7		0.805	SF
g0003056−295159	00:03:05.62	−29:51:59.3	11.741	0.0609	4	6.7	27.8			Aa
g0003130−355614	00:03:12.97	−35:56:13.4	10.508	0.0499	4	1.4	589.5	1123.4		Aa
g0003321−104441	00:03:32.13	−10:44:40.6	10.348	0.0299	4	8.0	2.5			Aae?
g0003449−204757	00:03:44.90	−20:47:56.5	12.314	0.0970	4	18.8	3.2		0.274	SF
g0004029−330202	00:04:02.86	−33:02:02.0	12.397	0.0380	4	12.9	2.4		0.447	SF?
g0004472−013413	00:04:47.22	−01:34:12.8	11.831	0.0239	4	5.1	9.9		0.843	SF
g0004517−060058	00:04:51.74	−06:00:57.6	12.722	0.1080	4	1.5	9.3			Aa
g0004576−014108	00:04:57.57	−01:41:07.9	12.569	0.0239	4	9.3	3.6			SF
g0005026−160715	00:05:02.58	−16:07:15.0	11.997	0.0339	4	13.8	2.2		0.268	SF
g0005028−274253	00:05:02.78	−27:42:52.5	11.619	0.0333	4	2.9	10.2		1.178	SF
g0005054−070536	00:05:05.37	−07:05:36.3	10.065	0.0128	4	2.6	12.9		1.038	SF

Column descriptions: (1) The target name of the object from the 6dFGS data base. (2) and (3) J2000 right ascension and declination of the object from the 2MASS XSC. (4) Total K-band magnitude calculated from 2MASS isophotal K magnitude according to equation (1) of Jones et al. (2004). (5) and (6) 6dFGS measured redshift and quality flag as described in Jones et al. (2004). Only redshifts with $Q \geqslant 3$ were deemed reliable. (7) The offset in arcsec from the NVSS radio position to the objects position in the 6dFGS data base. (8) The 1.4 GHz flux density in mJy from the NVSS catalogue. (9) The 843 MHz flux density in mJy for 6dFGS objects with a SUMSS catalogue match within 10 arcsec. (10) The *IRAS*–FSC 60 μm flux density in Jy for 6dFGS objects which also appear in additional target sample 126 (see Jones et al. 2004) of the 6dFGS. (11) The classification of the spectrum as defined in Table 2.

by $S^{5/2}$ such that counts in a static Euclidean universe would lie on a horizontal line. Counts determined for the radio-loud AGNs are plotted as filled circles and those for SF galaxies are plotted as open circles. The source counts of all 580 419 NVSS catalogue sources in the same region of sky as the 6dFGS–NVSS sample are shown as squares linked by a solid line. The counts follow an approximate power law between 1 Jy and 2.8 mJy, below which they fall sharply; this is because the NVSS catalogue becomes increasingly incomplete below 2.8 mJy (Condon et al. 1998). The vertical line at 2.8 mJy shown in the figure divides the two smallest bins of the AGN and SF samples. The same fall-off can be seen to the left-hand side of the vertical line in the counts of the AGN and SF subsamples indicating that this 6dFGS–NVSS sample is complete to a flux density limit of 2.8 mJy.

Radio source catalogues such as the NVSS are known to predominantly contain galaxies powered by radio-loud AGNs with a median redshift of $\tilde{z} \sim 0.8$ (Condon et al. 1998). In the much more nearby ($\tilde{z} \sim 0.05$) 6dFGS–NVSS sample the source counts of radio-loud AGNs follow roughly the same power-law slope as that of all radio sources but only account for roughly 1 per cent of their total number. The source counts of SF galaxies stay flat over the range 2.8 mJy to 1 Jy and therefore account for only 0.1 per cent of all sources at 1 Jy rising to 1–2 per cent of all sources at the survey limit. The counts of SF galaxies and radio-loud AGNs cross over at about 10 mJy, below which SF galaxies dominate the population of radio sources. At 1 Jy there are over 10 times more radio-loud AGNs than star formers, but the balance changes at lower flux density until at 2.8 mJy there are nearly 10 times more star formers than radio-loud AGNs in this volume-limited sample.

3.3 Redshift distribution

Fig. 6 shows the redshift distribution of 6dFGS–NVSS objects. The redshift distribution of all objects is shown in the bottom panel and separate distributions for SF galaxies and radio-loud AGNs are shown in the middle and top panels, respectively. The median redshift of all radio sources in the 6dFGS–NVSS sample is $\tilde{z} = 0.046$, very close to the median redshift ($\tilde{z} = 0.054$) of the underlying K-selected sample (Jones et al. 2004). SF galaxies dominate the lower redshift radio source population and are found at a median

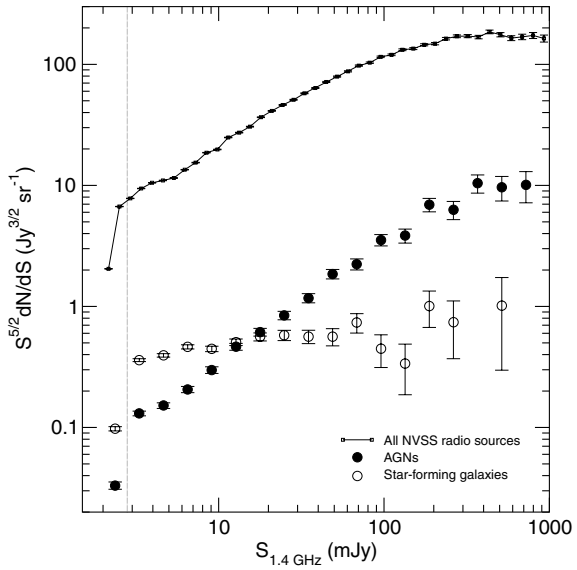

Figure 5. Differential source counts of 1.4-GHz NVSS sources multiplied by $S^{\frac{5}{2}}$ such that counts in a Euclidean universe would lie on a straight line. The source counts of all 580 419 NVSS sources in the region surveyed are shown by open squares linked by a solid line. AGN and SF class galaxies in the 6dFGS–NVSS sample are shown as filled and open circles, respectively. The error bars shown are the $\sqrt{n}$ counting uncertainties in each bin. A vertical line is plotted at $S_{1.4\,\mathrm{GHz}} = 2.8$ mJy which is the completeness limit of the 6dFGS–NVSS sample and is also the upper bound of the faintest bins calculated from the AGN and SF samples.

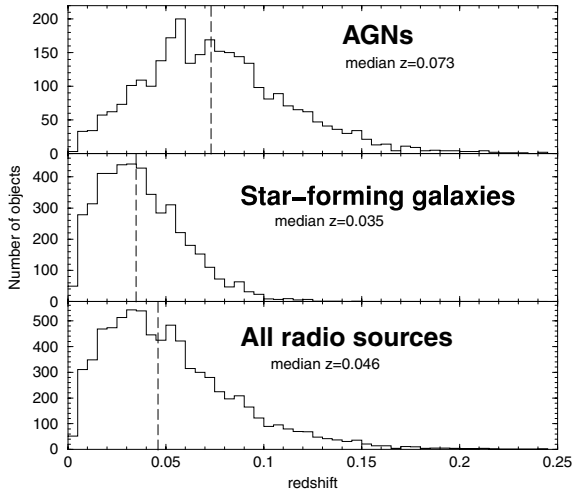

Figure 6. The redshift distribution of the 6dFGS–NVSS sample in bins of width 0.005 in redshift. Bottom panel: Redshift distribution of all 7824 objects for which a redshift has been measured. Middle panel: Redshift distribution of the 4625 SF galaxies. Top panel: Redshift distribution of the 2864 radio-loud AGNs. In each panel a vertical dashed line is drawn at the median redshift.

redshift of $\tilde{z} = 0.035$ while radio-loud AGNs dominate the higher redshift radio source population at a median redshift of $\tilde{z} = 0.073$.

The optical magnitude limits, radio flux density limits and median redshifts of other radio-optical samples, selected in a similar way to the 6dFGS–NVSS sample, are presented in Table 1. In their analysis of $S_{1.4\,\mathrm{GHz}} \geqslant 2.8$ mJy 2dFGRS–NVSS radio sources Sadler et al. (1999) found a median redshift of $\tilde{z} = 0.1$ for all 2dFGRS–NVSS galaxies, $\tilde{z} = 0.05$ for SF galaxies and $\tilde{z} = 0.14$ for radio-loud AGNs. The 2dFGRS goes more than two magnitudes deeper in b_J than the 6dFGS yet the median redshift of 2dFGRS–NVSS SF galaxies is only slightly higher than that found here for 6dFGS–NVSS galaxies, since it is primarily the radio flux density limit of optical-radio samples which limits the maximum distance to which SF galaxies can be found. In a survey of 2dFGRS–FIRST radio sources with a fainter flux density limit of $S_{1.4\,\mathrm{GHz}} \geqslant 1$ mJy, Magliocchetti et al. (2002) found a median redshift for SF galaxies of $\tilde{z} = 0.1$, more than twice that of the NVSS selected samples. Conversely, for radio-loud AGNs the median redshifts of the 2dFGRS–NVSS and 2dFGRS–FIRST samples are roughly similar ($\tilde{z} = 0.15$) whereas the median redshift of the 6dFGS–NVSS sample is significantly lower. This is a consequence of the different optical magnitude limits of the 6dFGS and the 2dFGRS; radio-loud AGNs fall out of both samples at the optical/NIR limit of the spectroscopy.

3.4 Detection rates

Fig. 7 shows the variation in the detection rate of 6dFGS–NVSS radio sources as a function of redshift. The detection rates were calculated by dividing the number of 6dFGS–NVSS galaxies in redshift bins of width 0.01 by the number of the 6dFGS DR2 primary targets with $Q = 3$ or 4 in each redshift bin. The average NVSS detection rate is shown as a dashed horizontal line and the median redshift of the 6dFGS–NVSS sample is shown as a dotted vertical line. The NVSS detection rate drops sharply from 34 per cent at $z = 0.005$ to just over 11 per cent at $z = 0.05$ (around the median redshift of the survey). It then rises steadily to over 20 per cent at $z = 0.15$ beyond which results are dominated by counting errors. This fall and subsequent rise in the detection rate with redshift can be explained in terms of the different redshift distributions of the SF and radio-loud AGN populations.

Below $z = 0.05$, SF galaxies dominate the radio source population and the detection rate is falling because of the 1.4 GHz flux density limit of the NVSS. SF galaxies have weaker radio powers and fewer

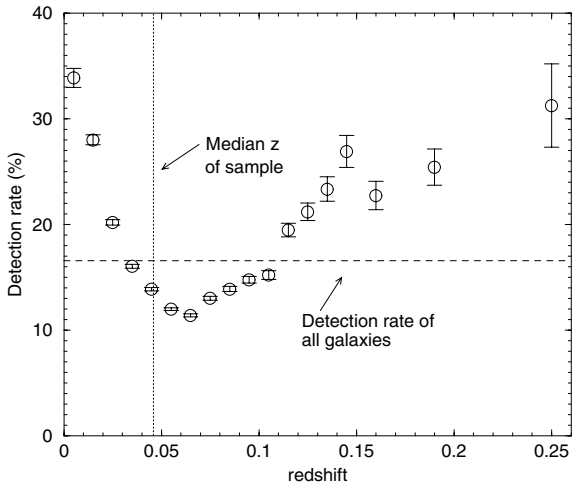

Figure 7. The NVSS detection rate of 6dFGS DR2 primary targets. Here the detection rate is defined as the percentage of radio identifications of 6dFGS DR2 objects for that bin. The error bars shown correspond to the $\sqrt{n}$ counting error in each bin. A vertical dotted line is plotted at the median redshift of the 6dFGS–NVSS sample and a horizontal dashed line is plotted at the overall radio detection rate of 16.5 per cent.

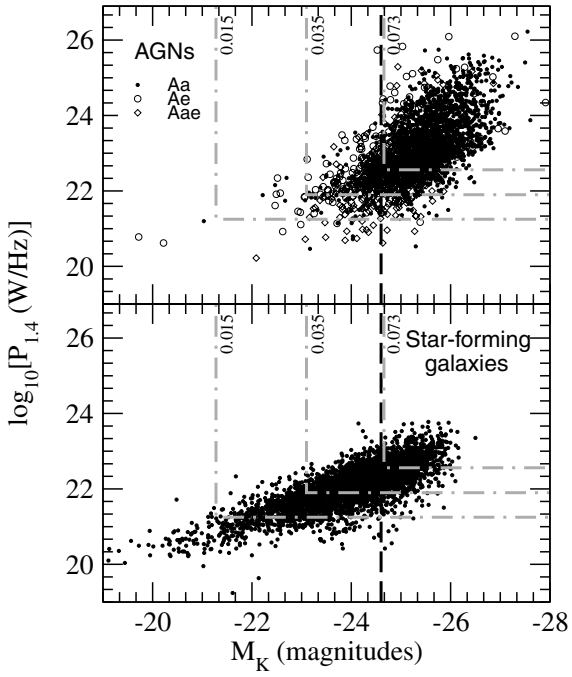

Figure 8. Bottom: 1.4 GHz radio power versus M_K for the 4625 SF galaxies in the 6dFGS–NVSS sample. Top: 1.4 GHz radio power versus M_K for the 2864 radio-loud AGNs in the 6dFGS–NVSS sample. Aa class AGNs are plotted as dots, Aae class AGNs are plotted as circles and Ae class AGNs are plotted as diamonds. A dashed vertical line is drawn at the value of $M_K^\star = -24.6$ mag from a Schechter function fit to the local K-band luminosity function of galaxies in the 6dFGS by Jones et al. (2006). The grey dot–dashed lines in each panel show the limiting values of $P_{1.4}$ and M_K derived from the radio ($S_{1.4\,\mathrm{GHz}} = 2.8$ mJy) and NIR ($K = 12.75$ mag) completeness limits of the 6dFGS–NVSS sample at the labelled redshifts (i.e. $z = 0.015, z = 0.035$, the median redshift of SF galaxies and $z = 0.073$, the median redshift of radio-loud AGNs). These lines show that the apparent correlation between $P_{1.4}$ and M_K is caused by the flux density and apparent magnitude limits and the range in redshift of the sample.

are found with increasing redshift because the limiting radio power of the 6dFGS–NVSS sample is increasing with redshift. Above $z = 0.05$, the detection rate is increasing and radio-loud AGNs dominate the radio source population. The population of radio-loud AGNs has a higher average radio power so they tend not to fall out of the sample because of the flux density limit of the NVSS. The $K \leqslant 12.75$ mag cut-off of the 6dFGS means that as redshift increases the galaxies left in the survey are on average more luminous in the NIR. Radio-loud AGNs preferentially reside within these most luminous galaxies (e.g. Fig. 8), resulting in an increase in the detection rate of radio-loud AGNs.

3.5 Luminosity distribution

Fig. 8 shows the 1.4 GHz monochromatic radio power ($P_{1.4}$, in units of W Hz^{-1}) versus the absolute K-band magnitude (M_K) for the radio-loud AGNs (top) and SF galaxies (bottom). Radio power measurements have been k-corrected using the usual form, $k_{\mathrm{radio}}(z) = (1+z)^{-(1+\alpha)}$ where α is the spectral index ($S_\nu \propto \nu^\alpha$). We determined median spectral indices separately for the AGN and SF classes by comparing the flux densities of the 436 galaxies that were also found in version 1.6 of the 843 MHz SUMSS catalogue (Mauch et al. 2003). For the 228 radio-loud AGNs the median spectral index was $\tilde{\alpha}_{843}^{1400} = -0.54 \pm 0.07$ and for the 208 SF galaxies the median spectral index was $\tilde{\alpha}_{843}^{1400} = -0.90 \pm 0.07$. These values of α have been applied to the k-corrections for all calculations of radio power throughout this paper. Both these values are close to the value of $\alpha = -0.7$ often assumed for radio source samples (e.g. Condon et al. 2002; Sadler et al. 2002). For most of the galaxies in this sample $k_{\mathrm{radio}}(z)$ is negligibly small.

In the K band, k-corrections [$k_K(z)$] are similar for galaxies of all Hubble types because different amounts of star formation in different galaxy types only significantly affect galaxy spectra at wavelengths shorter than 1 μm (Glazebrook et al. 1995; Cole et al. 2001). K-band k-corrections have been calculated following Glazebrook et al. (1995) who derived $k_K(z)$ from the evolutionary synthesis models of Bruzual & Charlot (1993) assuming an instantaneous burst of star formation at age 5 Gyr. At the small redshifts probed by this dataset ($z < 0.2$), $k_K(z)$ never changes M_K by more than 0.4 mag.

The SF galaxies in Fig. 8 span a range of M_K between −20 and −26, they have median $\tilde{M}_K = -24.13$, lower than $M_K^\star$. SF galaxies, with median $\log[\tilde{P}_{1.4}\,(\mathrm{W\,Hz^{-1}})] = 22.13$, have weaker radio powers ($P_{1.4} < 10^{23}\,\mathrm{W\,Hz^{-1}}$) than radio-loud AGNs. Radio-loud AGNs are almost all found in objects brighter than $M_K^\star$, indicative of their preferential location in the brightest galaxies. The median $\tilde{M}_K$ of radio-loud AGNs is −25.40 and they have median radio power $\log[\tilde{P}_{1.4}\,(\mathrm{W\,Hz^{-1}})] = 23.04$, almost an order of magnitude brighter than the median radio power of SF galaxies. Though SF galaxies have lower radio powers, radio-loud AGNs span a wide range in radio power from 10^{21} to $10^{26}\,\mathrm{W\,Hz^{-1}}$, indicating that there is no clear observational regime in which SF galaxies can be separated from radio-loud AGNs purely on the basis of radio power.

4 THE FIR–RADIO CORRELATION

It has been well established that a correlation exists between FIR and radio continuum emission from normal galaxies (see Helou, Soifer & Rowan-Robinson 1985; Condon, Anderson & Helou 1991; Condon 1992; Condon & Broderick 1988). This correlation has been attributed to ongoing star formation within the host galaxy, where radio continuum emission is produced by a combination of synchrotron emission from electrons accelerated in the supernova remnants of short-lived massive stars ($M > 8\,\mathrm{M}_\odot$ with lifetimes $<3 \times 10^7$ yr) and free–free emission from H II regions ionized by these same massive stars (Condon 1992). FIR emission is caused by thermal reradiation of dust in H II regions heated by this same population of massive stars. Though it is understood that recent star formation is the process which drives both the radio continuum and FIR emission of galaxies which lie on the correlation, the actual mechanism that relates non-thermally dominated radio power and thermally dominated FIR luminosity is poorly understood.

The FIR–radio correlation has served as a diagnostic tool for large samples of radio sources, as it can be used to distinguish between galaxies with ongoing star formation and those harbouring a radio-loud AGN. Galaxies falling on the correlation derive their radio emission from star formation, whereas galaxies with a radio 'excess' above that expected from the correlation derive their radio emission from the presence of a radio-loud AGN (e.g. Condon & Broderick 1988; Condon et al. 2002). The correlation also constrains models relating star formation rate to radio power (Condon 1992). In this section results from analysis of the population of radio sources in the 6dFGS–NVSS sample with FIR detections in the *IRAS*–FSC are presented, both as a consistency check for the spectral classification

of the sample and to examine the correlation for a large sample of normal galaxies.

4.1 Finding *IRAS* Detections

In addition to the primary *K*-selected sample, the 6dFGS aims to measure redshifts for several additional target samples selected at various wavelengths. One of these additional target lists consists of $\sim 11\,000$ *IRAS*–FSC galaxies selected at 60 μm from the *IRAS*–FSC (For a complete description of the 6dFGS additional target samples see Jones et al. 2004). Much of this *IRAS*–FSC additional target sample (which we call the 6dFGS–FSC sample) overlaps with our 6dFGS–NVSS sample. It is therefore straightforward to find *IRAS*–FSC detections of 6dFGS–NVSS primary target objects by cross-matching their 6dF target ID names. 4403 6dFGS–FSC targets were observed in the DR2. Table 4 shows the spectral classification of the 2942 galaxies which are common to the 6dFGS–NVSS sample and the 6dFGS–FSC sample. Predominantly emission-line (i.e. Ae, Aae, SF) galaxies are detected in the FIR as has been observed in other spectroscopic studies of FIR selected galaxies (e.g. Lawrence et al. 1986; de Grijp et al. 1992; Sadler et al. 2002). The four Aa galaxies detected in the 6dFGS–NVSS–FSC subsample have low S/N and may have been misclassified.

Condon et al. (2002) noted that the FIR–radio correlation ensures that most FIR sources powered by ongoing star formation are also radio sources and vice versa. The FIR/radio ratio $u = \log(S_{60\,\mu\mathrm{m}}/S_{1.4\,\mathrm{GHz}})$ for nearby spiral galaxies in the UGC has a mean value of $\langle u \rangle = 2.05 \pm 0.02$ with rms width $\sigma_u = 0.2$ (Condon & Broderick 1988). This value of $\langle u \rangle$ happens to be the ratio between the 280 mJy flux density limit of the *IRAS*–FSC at 60 μm and the limit of the NVSS at 1.4 GHz ($u \approx 2.05$). 58.1 per cent of spectroscopically classified SF galaxies have 6dFGS–FSC detections leaving 929 SF galaxies with no FIR detection. These missing detections are the result of incompleteness at the flux density limits of the 6dFGS–FSC and 6dFGS–NVSS samples and incomplete sky coverage of the region $-40^\circ < \delta < 0^\circ$ in the *IRAS*–FSC (Moshir et al. 1993).

When available, 100 μm flux densities from the *IRAS*–FSC were also obtained for each 6dFGS–FSC source. For the ∼20 per cent of objects which did not have a 100 μm detection the 100 μm flux density was assumed to be twice the 60 μm flux density based on the calculated average $\langle \log(S_{100\,\mu\mathrm{m}}/S_{60\,\mu\mathrm{m}}) \rangle = 0.3$ with a scatter of 0.2 from the bright galaxy sample of Soifer et al. (1989). 60 and 100 μm flux densities are then converted into the quantity FIR (in units of W m^{-2}) defined by

$$\mathrm{FIR} = 1.26 \times 10^{-14} \left(2.58 S_{60\,\mu\mathrm{m}} + S_{100\,\mu\mathrm{m}}\right) \quad (1)$$

Table 4. Spectral classification of 6dFGS–NVSS objects which are also found in the 6dFGS–FSC sample.

Spectral class	$N^{\mathrm{6dFGS-FSC}\,a}_{\mathrm{6dFGS-NVSS}}$	Per cent of total[b]
SF	2690	58.1
Ae	138	37.3
Aae	66	17.8
Aa	4	0.2
Star	2	14.3
?	42	13.1
Total	2942	37.6

[a]The number of 6dFGS DR2 objects which are common to both the *IRAS*–FSC and the NVSS catalogue.
[b]The percentage of 6dFGS–NVSS objects that are also 6dFGS–FSC objects.

where $S_{60\,\mu\mathrm{m}}$ and $S_{100\,\mu\mathrm{m}}$ are in Janskys (Helou et al. 1985). FIR is a measure of the total FIR flux between 42.5 and 122.5 μm.

4.2 The FIR–radio ratio *q*

The radio–FIR correlation is often parametrized by the FIR–radio flux ratio parameter q (Helou et al. 1985). This is defined by

$$q = \log\left[\frac{\mathrm{FIR}/(3.75 \times 10^{12})}{S_{1.4\,\mathrm{GHz}}}\right], \quad (2)$$

where FIR (defined by equation 1) is divided by the factor 3.75×10^{12} Hz (the frequency at 80 μm) to convert FIR to W m^{-2} Hz^{-1}. The mean value of $\langle q \rangle = 2.28$ with rms scatter $\sigma_q = 0.22$ for all 2411 objects with measured flux densities at both 60 and 100 μm. σ_q is somewhat larger than the value found by Condon et al. (2002) for a more nearby sample of UGC–NVSS galaxies. This discrepancy reflects the large uncertainties associated with fainter *IRAS*–FSC flux densities as well as the larger radio-loud AGN population contained in the present sample. For the subset of 2242 SF galaxies with measured 60 and 100 μm flux densities $\langle q_{\mathrm{SF}} \rangle = 2.3$ with rms scatter $\sigma_{\mathrm{SF}} = 0.18$, in close agreement with Condon et al. (2002) for the UGC–NVSS sample. This value also agrees well with results from samples of stronger *IRAS* sources in spiral galaxies (Condon et al. 1991). For the subset of 169 radio-loud AGNs with measured 60 and 100 μm flux densities $\langle q_{\mathrm{AGN}} \rangle = 2.0$ with rms scatter $\sigma_{\mathrm{AGN}} = 0.5$. The larger scatter is expected for radio-loud AGNs as these are not expected to be correlated as strongly and the smaller average q value is caused by the stronger flux densities of radio-loud AGNs.

A cut-off of $q = 1.8$ is often used as a diagnostic to distinguish between SF galaxies and radio-loud AGNs (e.g. Condon et al. 2002), and it appears that the spectroscopic classification of radio sources used in this work agrees well with this diagnostic. Only 10 (<1 per cent) of the SF galaxies in the combined 6dFGS–NVSS–FSC sample have $q < 1.8$, the value below which a galaxy is three times more radio-loud than the mean for SF galaxies. These 10 galaxies may come from a class of 'composite' radio source, whose radio emission is a mixture of both SF and radio-loud AGN activity or they may be candidate 'taffy' galaxy pairs which recently suffered a direct collision (e.g. Condon et al. 1993). The SF spectral classification of these objects is retained in further analysis.

4.3 Far-infrared colours

Another diagnostic which can be used to distinguish between radio-loud AGNs and SF galaxies is the FIR spectral index between 60 and 25 μm, $\alpha_{\mathrm{IR}} = \log(S_{25\,\mu\mathrm{m}}/S_{60\,\mu\mathrm{m}})/\log(60/25)$. α_{IR} is a measure of the temperature of the FIR emitting dust. SF galaxies have cooler ($T < 50$ K) dust emission because of their extended star and gas distributions and therefore have values of $\alpha_{\mathrm{IR}} < -1.5$. The central engines of AGNs heat the dust to warmer temperatures ($T > 100$ K) and have values of $\alpha_{\mathrm{IR}} > -1.5$ (de Grijp et al. 1992).

60 radio-loud AGNs and 769 SF galaxies in the sample were detected in the *IRAS*–FSC at 25 μm. Fig. 9 plots α_{IR} versus q for these galaxies, comparing the dust temperature of each galaxy with its degree of radio excess. The vast bulk of SF galaxies lie in the lower right-hand side of the plot as expected from the radio–FIR correlation. The majority of radio-loud AGNs have $\alpha_{\mathrm{IR}} > -1.5$ (many lie outside the boundary on the upper left-hand side of Fig. 9) indicating that the FIR spectral index, used in concert with the radio–FIR correlation agrees well with spectral classification as a discriminator of SF galaxies and radio-loud AGNs.

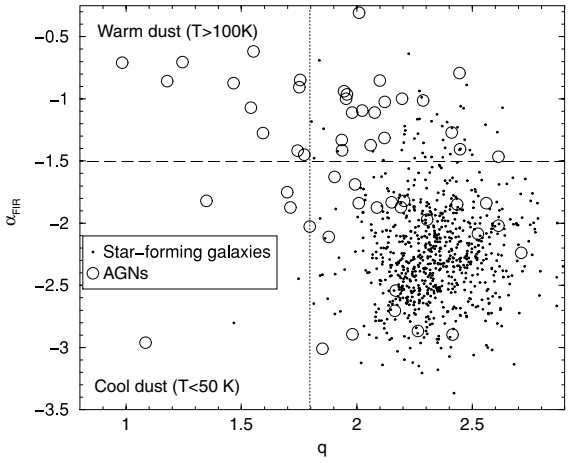

Figure 9. $\alpha_{\rm FIR}$ versus q (defined by equation 2) for the 769 SF galaxies (dots) and the 60 radio-loud AGNs (circles) in the combined 6dFGS–NVSS–FSC sample which also had a detection in the *IRAS*–FSC at 25 „ m. A dashed horizontal line is shown at $\alpha_{\rm FIR} = -1.5$ to delineate the regions occupied by 'warm' ($\alpha_{\rm FIR} > -1.5$) and 'cool' ($\alpha_{\rm FIR} < -1.5$) *IRAS* galaxies. The canonical value of $q = 1.8$, used to distinguish SF galaxies from AGNs in other surveys (e.g. Condon et al. 2002) is shown as a dotted vertical line.

4.4 Composite optical spectra and *IRAS* comparisons

For about 90 per cent of the radio-detected 6dFGS galaxies in Table 3, a classification as either AGNs or SF (as discussed in Section 2.5) appears straightforward. Most of the galaxies we have classified as SF are detected by *IRAS*, and almost all of them lie in the lower right-hand quadrant of Fig. 9, as expected if their FIR emission arises from dust heated in SF regions. In contrast, the *IRAS* detection rate of the objects classified as Aa in Table 3 is close to zero, as expected if their inner regions are largely free of gas and dust and their radio emission comes exclusively from an AGN.

For the 10 per cent of galaxies in Table 3 which show optical emission lines with ratios characteristic of an AGN, and which are therefore classified as Aae or Ae, the situation is less clear-cut. As discussed by Best et al. (2005b), a possible problem with spectral classification of emission-line AGNs as radio-loud is that emission-line AGN activity is often be accompanied by star formation (Kauffmann et al. 2003). Even if the AGN is radio-quiet, this associated star formation will give rise to radio emission. For any such galaxy included in the sample, the origin of the radio emission will be star formation, but the optical spectrum could still be dominated by emission lines from a (radio-quiet) AGN, leading us to classify the object as Aae or Ae.

Although the present data are insufficient to disentangle the separate contributions from star formation and the AGN to the radio emission from these galaxies, we can estimate what fraction of them might have been misclassified spectroscopically by comparing our spectroscopic classification with the radio–FIR diagnostic. High resolution very long baseline interferometry (VLBI) imaging of these sources may be used to distinguish the parsec-scale AGN components of these galaxies from the kpc scale radio structure resulting from star formation (e.g. Norris et al. 1992). Such observations are outside the scope of the present paper.

20 spectroscopically classified AGNs in the 6dFGS–NVSS sample lie in the lower right-hand region of Fig. 9 and would be classified as SF galaxies by the radio–FIR diagnostic. This implies that about 1/3 of all spectroscopically classified emission-line AGNs (Ae and Aae class) in the 6dFGS–NVSS sample (∼250) fail the radio–FIR diagnostic. It is probable that some of these may be genuinely misclassified as radio-loud AGNs from their optical spectra and derive the majority of their radio emission from star formation. Assuming that all absorption-line radio-loud AGNs (Aa class) have been correctly classified, the disagreement between spectroscopic classification and the radio–FIR diagnostic for 6dFGS–NVSS AGNs is ∼10 per cent. We estimated a similar reliability for our classification scheme in Section 2.5 from repeated visual inspection of the spectra. It is clear that difficulties in classifying emission-line spectra with composite or borderline AGN + SF properties are the primary cause of misclassification of radio sources in our sample. We believe that this is a worst case estimate of the reliability of our spectroscopic classification and note that on the whole the spectroscopic classification technique agrees well with the radio–FIR correlation diagnostic.

Only 38 per cent of objects in the 6dFGS–NVSS sample were detected in the 6dFGS–FSC sample. This makes the radio–FIR correlation diagnostic unsuitable for the sample presented in this paper because a non-detection of a galaxy in the 6dFGS–FSC sample does not preclude it from being a SF galaxy in the 6dFGS–NVSS sample. Deeper wide-angle FIR surveys are required to detect SF galaxies out to the redshifts probed by the current generation of optical redshift surveys.

4.5 The FIR–radio correlation of 6dFGS galaxies

Fig. 10 shows the radio–FIR correlation ($P_{1.4}$ versus $L_{\rm FIR}$) of 6dFGS–NVSS galaxies with a 60 μm detection in the *IRAS*–FSC. Spectroscopically classified AGNs are plotted as circles and SF galaxies are plotted as dots. The SF galaxies show a strong correlation between radio power and FIR luminosity extending over four orders of magnitude though the scatter tends to increase above $L_{\rm FIR} = 10^{11}$ $L_{\odot}$ as was seen for *IRAS*–FSC detected galaxies in the 2dFGRS–NVSS sample of Sadler et al. (2002). The FIR luminosities show less correlation with radio power for radio-loud AGNs; these are found across the whole range of FIR luminosity sampled. Many of them have 'excess' radio powers, causing them to lie above the correlation defined by the SF galaxies. These radio-excess *IRAS*

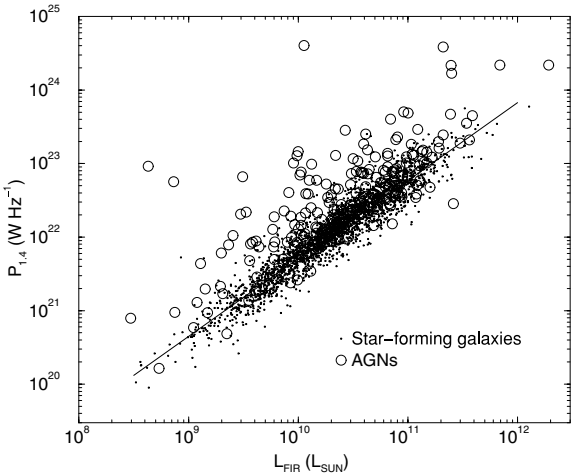

Figure 10. The radio–FIR correlation of all 2690 SF galaxies (dots) and 208 radio-loud AGNs (open circles) in the combined 6dFGS–NVSS–FSC sample. A best-fitting line (equation 3 in the text) based on a subsample of 2242 SF galaxies with accurate 60 and 100 „ m flux densities is also shown.

galaxies are of interest for understanding the connection between star formation and AGNs in galaxies (Drake et al. 2003).

A least-squares line of best fit to the subsample of 2242 SF galaxies for which accurate 60 and 100 μm flux densities are available in the *IRAS*–FSC is also shown in Fig. 10. The line has the form

$$\log(P_{1.4}) = (1.06 \pm 0.01)\log(L_{\rm FIR}) + (11.11 \pm 0.1), \quad (3)$$

which is similar to that found in other derivations of the radio–FIR correlation for brighter galaxies (e.g. Devereux & Eales 1989; Condon et al. 1991; Condon & Broderick 1988).

4.6 Ultraluminous infrared galaxies

Ultraluminous infrared galaxies (ULIRGs) with $L_{\rm FIR} > 10^{12}\,{\rm L}_{\odot}$ which are powered by a mixture of starburst activity and an AGN (Sanders & Mirabel 1996) are of interest for understanding the starburst–AGN connection. There are two ULIRGs in the present sample; such objects are extremely rare in the local Universe. The nearest known (Arp 220) has redshift 0.018. The local ULIRG space density, estimated from the FIR luminosity function of Saunders et al. (1990), is $< 10^{-8}$ Mpc^{-3}. The enclosed volume of the 6dFGS–NVSS sample (see Table 1) is $\sim 3.9 \times 10^{8}$ Mpc^{3}, meaning that less than four ULIRGs are expected in the 6dFGS–NVSS volume. Interestingly, Sadler et al. (2002) found seven ULIRGs in the 2dFGRS–NVSS sample, in a volume of 5.0×10^{7} Mpc^{3} in the redshift range $0.15 < z < 0.3$, which implies their space density is 1.4×10^{-7} Mpc^{-3} within the more distant 2dFGRS redshift range. This suggests that these objects evolve strongly with redshift and is consistent with their measured evolution of $(1 + z)^{7}$ between $0 < z < 1$ (Cowie et al. 2004; Sanders 2004).

5 THE LOCAL RADIO LUMINOSITY FUNCTION

The luminosity function [$\Phi(P)$] of a sample of astronomical objects is a measure of the variation in their space density with luminosity. The *local* RLF is the global average space density of radio sources at the present epoch (Auriemma et al. 1977; Condon 1989). An accurate derivation of the local RLF is important as a present epoch benchmark for studies of the population of radio sources at higher redshift so that their cosmological evolution can be determined. In this section we derive the local RLF for the 6dFGS–NVSS sample as a whole and for the SF galaxy and radio-loud AGN subgroups separately.

5.1 Completeness

The RLF can be calculated directly but requires a sample which is complete to the limits of all the surveys from which it is derived. We therefore must define a subsample of the 6dFGS–NVSS sample which is complete to both its *K*-band magnitude limit and 1.4 GHz flux density limit. In the *K* band, the 2MASS XSC from which the 6dFGS primary sample is selected is complete and reliable well below the $K = 12.75$ mag limit of the 6dFGS (Jarrett et al. 2000; Jones et al. 2006). The 6dFGS primary sample may also miss populations of radio sources in the local Universe either because their hosts appear stellar on optical plates (e.g. QSOs, BL Lacs or compact galaxies) or because they are too blue in colour to be detected in the 6dFGS primary sample (e.g. Seyfert galaxies). A selection of such objects was observed as additional targets during the 6dFGS under programme ID 125 (Jones et al. 2004). A full analysis of them will be the subject of a future paper.

The sharp drop in the source counts of NVSS radio sources below 2.8 mJy (Fig. 5) indicates that the NVSS catalogue is incomplete below this limit. We applied a 1.4 GHz flux density limit of 2.8 mJy to the 6dFGS–NVSS sample when calculating the RLF. The same flux density limit was used by Sadler et al. (2002) to measure the luminosity function of 2dFGRS–NVSS radio sources. There are 6961 6dFGS–NVSS galaxies with $S_{1.4\,\rm GHz} \geqslant 2.8$ mJy, $K \leqslant 12.75$ of which 6667 have 6dFGS DR2 measured redshift $z > 0.003$. Of these, 3997 were assigned spectral class SF, 2652 were assigned AGNs and 18 were unclassified. These 18 unclassified spectra with measured redshifts were classified on the basis of their measured radio power: those with $P_{1.4} \leqslant 10^{23}$ W Hz^{-1} (9) were classed as SF and those with $P_{1.4} > 10^{23}$ W Hz^{-1} (9) were classed as AGNs.

We corrected the measured luminosity function for incomplete sampling of the celestial sphere by the 6dFGS DR2 and for spectroscopic incompleteness of the 6dFGS–NVSS sample. To account for incomplete sampling of the celestial sphere we normalized all volumes by the effective area of the 6dFGS–NVSS sample derived in Section 2.3. Of the 6961 6dFGS–NVSS objects meeting our selection criteria, 280 had spectra which were too poor in quality to determine a redshift and 14 were associated with galactic stars. The poor quality spectra arose for a myriad of reasons which were primarily instrumental (e.g. broken fibres, misplaced buttons, etc.) and are expected to be a random subset of the data. The spectroscopic incompleteness of 4 per cent causes the luminosity function to be underestimated, so values of $\Phi(P_{1.4})$ have been increased by 4 per cent to compensate.

5.2 Calculating the luminosity function

We have measured the RLF using the $1/V_{\rm max}$ method of Schmidt (1968). $V_{\rm max}$ is the maximum volume in which a galaxy will satisfy all of the sample selection criteria, which in the case of the 6dFGS–NVSS sample are $S_{1.4\,\rm GHz} \geqslant 2.8$ mJy, $K \leqslant 12.75$ mag and $z > 0.003$.

We have corrected the measured RLF for galaxy clustering at a distance *s* centred on our own Galaxy using

$$\frac{\rho_{\rm P}}{\rho} = 1 + \frac{3}{3 - \gamma_{\rm s}}\left(\frac{s_0}{s}\right)^{\gamma_{\rm s}} \quad (4)$$

(Peebles 1980), as discussed by Condon et al. (2002). Here $\rho_{\rm P}/\rho$ is the expected overdensity near our own Galaxy, or the space density ($\rho_{\rm P}$) of *local* galaxies divided by the average space density (ρ) of *all* galaxies, $\gamma_{\rm s}$ is the slope and s_0 the correlation scale length from a power-law fit, $\xi(s) = (s/s_0)^{-\gamma_{\rm s}}$, of the two-point correlation function in redshift space. The two-point correlation function of local radio sources has been derived from a subset of the 6dFGS–NVSS sample (Mauch 2006), and is adequate to describe clustering of radio sources centred on our own galaxy. Derivations of $\gamma_{\rm s}$ and s_0 for radio sources in the 6dFGS–NVSS sample yielded values of $\gamma_{\rm s} = 1.57$ and $s_0 = 10.07$. $\xi(s)$ has a power-law form for distances $s < 30$ Mpc, and $\xi(s) \approx 0$ for $s > 30$ Mpc. Therefore to correct for the local overdensity, we have multiplied the volume within *s* by equation (4) to calculate $V_{\rm max}$ for $s < 30$ Mpc. In practice, $V_{\rm max}$ is always much larger than the local clustering volume, and so this correction has made little difference to the results.

5.3 Results

Table 5 lists the measured local RLF for the SF galaxies, radio-loud AGNs and the 6dFGS–NVSS sample as a whole. The 4006 SF galaxies have $\langle V/V_{\rm max}\rangle = 0.509 \pm 0.005$, the 2661 radio-loud AGNs have $\langle V/V_{\rm max}\rangle = 0.532 \pm 0.006$ and all the 6667 radio sources in the

Table 5. Local RLFs at 1.4 GHz for the radio-loud AGNs, SF galaxies and for all radio sources.

	All galaxies		SF galaxies		Radio-loud AGNs	
$\log_{10} P_{1.4}$ (W Hz^{-1})	N	$\log \Phi$ (mag^{-1} Mpc^{-3})	N	$\log \Phi$ (mag^{-1} Mpc^{-3})	N	$\log \Phi$ (mag^{-1} Mpc^{-3})
20.0	3	$-2.90^{+0.20}_{-0.39}$	3	$-2.90^{+0.20}_{-0.39}$		
20.4	46	$-2.52^{+0.08}_{-0.10}$	43	$-2.56^{+0.09}_{-0.11}$	3	$-3.63^{+0.23}_{-0.54}$
20.8	116	$-2.84^{+0.04}_{-0.05}$	103	$-2.89^{+0.04}_{-0.05}$	13	$-3.77^{+0.11}_{-0.15}$
21.2	319	$-2.82^{+0.02}_{-0.03}$	296	$-2.85^{+0.03}_{-0.03}$	23	$-4.01^{+0.09}_{-0.11}$
21.6	654	$-3.00^{+0.02}_{-0.02}$	589	$-3.05^{+0.02}_{-0.02}$	65	$-4.04^{+0.05}_{-0.06}$
22.0	1266	$-3.25^{+0.01}_{-0.01}$	1106	$-3.31^{+0.01}_{-0.01}$	160	$-4.18^{+0.04}_{-0.04}$
22.4	1496	$-3.68^{+0.01}_{-0.02}$	1119	$-3.79^{+0.02}_{-0.02}$	377	$-4.35^{+0.03}_{-0.03}$
22.8	1138	$-4.23^{+0.02}_{-0.02}$	588	$-4.45^{+0.02}_{-0.02}$	550	$-4.62^{+0.02}_{-0.03}$
23.2	658	$-4.78^{+0.02}_{-0.02}$	133	$-5.36^{+0.04}_{-0.05}$	525	$-4.91^{+0.03}_{-0.03}$
23.6	378	$-5.06^{+0.03}_{-0.03}$	26	$-6.12^{+0.11}_{-0.14}$	352	$-5.09^{+0.03}_{-0.03}$
24.0	259	$-5.36^{+0.03}_{-0.03}$			259	$-5.36^{+0.03}_{-0.03}$
24.4	183	$-5.57^{+0.04}_{-0.04}$			183	$-5.57^{+0.04}_{-0.04}$
24.8	81	$-6.03^{+0.06}_{-0.07}$			81	$-6.03^{+0.06}_{-0.07}$
25.2	49	$-6.33^{+0.08}_{-0.09}$			49	$-6.33^{+0.08}_{-0.09}$
25.6	16	$-6.74^{+0.16}_{-0.27}$			16	$-6.74^{+0.16}_{-0.27}$
26.0	3	$-7.30^{+0.25}_{-0.68}$			3	$-7.30^{+0.25}_{-0.68}$
26.4	2	$-8.12^{+0.27}_{-0.85}$			2	$-8.12^{+0.27}_{-0.85}$
Total	6667		4006		2661	
$\langle V/V_{\rm max}\rangle$	0.518 ± 0.004		0.509 ± 0.005		0.532 ± 0.006	

combined sample have $\langle V/V_{\rm max}\rangle = 0.518 \pm 0.004$. The $\langle V/V_{\rm max}\rangle$ value for radio-loud AGNs is more than 3σ from the value of 0.5 expected if there were no significant clustering or evolution in the sample. Some evolution of the radio-loud AGN population is probable over the 1–2 Gyr look-back time of the 6dFGS–NVSS sample. The local RLF of all 6dFGS–NVSS galaxies is shown in Fig. 11; its statistical errors are of order 1 per cent or less over five decades of radio luminosity. Separate local RLFs for both SF galaxies and radio-loud AGNs are shown in Fig. 12. These cross over at $P_{1.4} = 10^{23}$ W Hz^{-1}, SF galaxies dominate the population of radio sources below this power and radio-loud AGNs dominate the population above it.

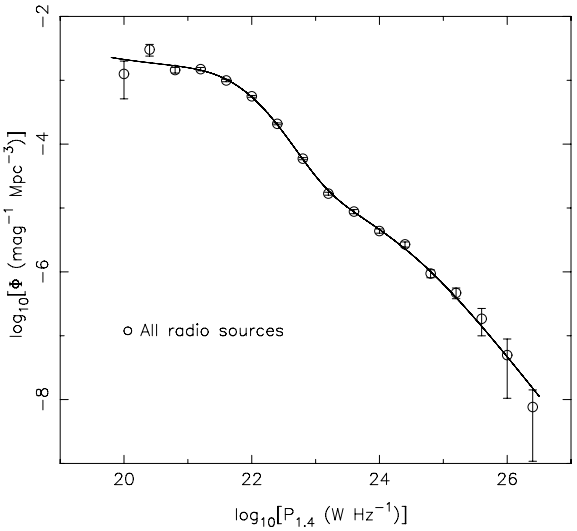

Figure 11. The local luminosity function at 1.4 GHz measured from all the radio sources in the 6dFGS–NVSS sample. The curve is the sum of the contributions to the luminosity function from fits of equations (5) and (6) to the SF and AGN data, respectively.

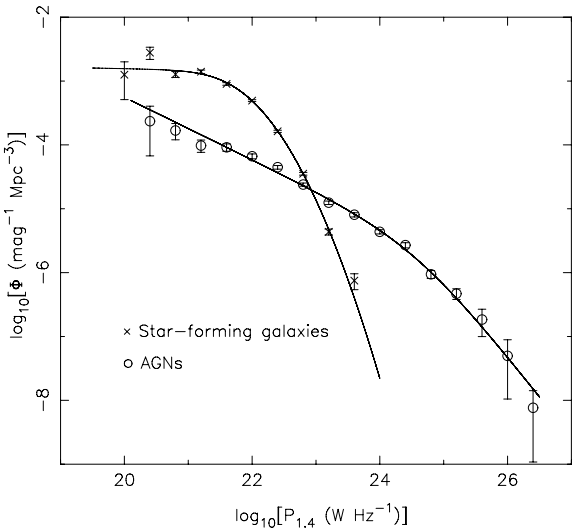

Figure 12. The local luminosity function at 1.4 GHz derived separately for the radio-loud AGNs (circles) and SF galaxies (crosses) in the 6dFGS–NVSS sample. The two curves are the fits of equations (5) and (6) to the SF and AGN data, respectively.

Galaxy luminosity functions are commonly fitted by the Schechter function (Schechter 1976). This function turns over more steeply towards high luminosities than RLFs of SF galaxies. Instead the RLF is commonly fitted by the parametric form given by

$$\Phi(P) = C \left(\frac{P}{P_\star}\right)^{1-\alpha} \exp\left\{-\frac{1}{2}\left[\frac{\log_{10}(1+P/P_\star)}{\sigma}\right]^2\right\}, \qquad (5)$$

as was used to fit the luminosity function of *IRAS* galaxies by Saunders et al. (1990). The best-fitting parameters of equation (5) for 6dFGS–NVSS SF galaxies are

$C = 10^{-2.83\pm0.05}\,\mathrm{mag^{-1}\,Mpc^{-3}}$;

$P_\star = 10^{21.18\pm0.22}\,\mathrm{W\,Hz^{-1}}$;

$\alpha = 1.02 \pm 0.15$;

$\sigma = 0.60 \pm 0.04$.

Equation (5) is inadequate to describe the RLF of radio-loud AGNs and we have instead fitted these data with a two power-law function analogous to the optical luminosity function of quasars:

$$\Phi(P) = \frac{C}{(P_\star/P)^\alpha + (P_\star/P)^\beta} \qquad (6)$$

(Dunlop & Peacock 1990; Brown et al. 2001). The best-fitting parameters of equation (6) for 6dFGS–NVSS radio-loud AGNs are:

$C = 10^{-5.50\pm0.25}\,\mathrm{mag^{-1}\,Mpc^{-3}}$;

$P_\star = 10^{24.59\pm0.30}\,\mathrm{W\,Hz^{-1}}$;

$\alpha = 1.27 \pm 0.18$;

$\beta = 0.49 \pm 0.04$.

The curves plotted in Fig. 12 show the fits of equations (5) and (6) to the SF galaxies and radio-loud AGNs, respectively. The RLF of all 6dFGS–NVSS galaxies is the sum of the two contributions from SF galaxies and radio-loud AGNs, as shown in Fig. 11. The curve in this figure is the sum of the two separate fits to the RLF for the SF galaxies and radio-loud AGNs.

5.4 Discussion

The RLF of active galaxies maintains a power-law form for about five orders of magnitude before turning over above $P_{1.4} > 10^{24.5}\,\mathrm{W\,Hz^{-1}}$. This power-law form of the radio-loud AGN luminosity function can only continue to fainter powers if it does not exceed the space density of the luminous galaxies in which radio-loud AGNs preferentially reside. Taking the best-fitting Schechter function to the B-band luminosity for early-type galaxies in the 2dFGRS from Madgwick et al. (2002), and assuming that radio-loud AGNs typically live in the brightest early-type galaxies (see Fig. 8, top), the space density of early-type galaxies with ($L_B > L_B^\star$) is $(9.3 \pm 0.3) \times 10^{-4}\,\mathrm{Mpc^{-3}}$ (for $H_0 = 70\,\mathrm{km\,s^{-1}\,Mpc^{-1}}$). The space density of radio-loud AGNs with $P_{1.4} > 10^{20.2}\,\mathrm{W\,Hz^{-1}}$ from the 6dFGS–NVSS luminosity function of Fig. 12 is $\approx 8 \times 10^{-4}\,\mathrm{Mpc^{-3}}$. If the power-law form for radio-loud AGNs continues to fainter radio powers a maximum must be reached at $P_{1.4} \approx 10^{19.5}\,\mathrm{W\,Hz^{-1}}$, just beyond the limit of the present data. Though there is some evidence (e.g. from Fig. 8) that radio-loud AGNs of lower radio power may live in less luminous host galaxies which have higher space density.

In recent models, in which the radio-loud AGN luminosity function is interpreted as the distribution of the time spent by an AGN at a given radio power, the strong variability of radio-loud AGNs is related to the heating of cooling flows in galaxies and clusters (e.g. Nipoti & Binney 2005; Best et al. 2006). From a fit to the RLF of 2dFGRS–FIRST radio sources, Nipoti & Binney (2005) predict that the AGN luminosity function will turn over at $P_{1.4} = 10^{20.4\pm0.1}\,\mathrm{W\,Hz^{-1}}$, just at the faint limit of the 6dFGS–NVSS luminosity function. Such models are poorly constrained by observational data at present and require further constraints on the relationship between the mechanical luminosity of heating of cooling flows by radio jets in AGNs as well as a more detailed understanding of the X-ray luminosity function of AGNs.

5.5 Comparison of recent RLF measurements

Fig. 13 shows a comparison of the RLFs of 6dFGS–NVSS galaxies with those of UGC–NVSS galaxies and 2dFGRS–NVSS galaxies. Values of the 2dFGRS–NVSS luminosity function have been shifted from their published values to $H_0 = 70\,\mathrm{km\,s^{-1}\,Mpc^{-1}}$. The properties of these three surveys are compared in Table 1. We make no comparison of our measured RLF with that measured from SDSS–NVSS/FIRST galaxies because the normalization of the SDSS–NVSS/FIRST RLF is tied to the 2dFGRS–NVSS RLF which it follows very closely over the complete range of radio powers sampled (Best et al. 2005b). We also do not make any comparison with the 2dFGRS–FIRST RLF because the FIRST survey is insensitive

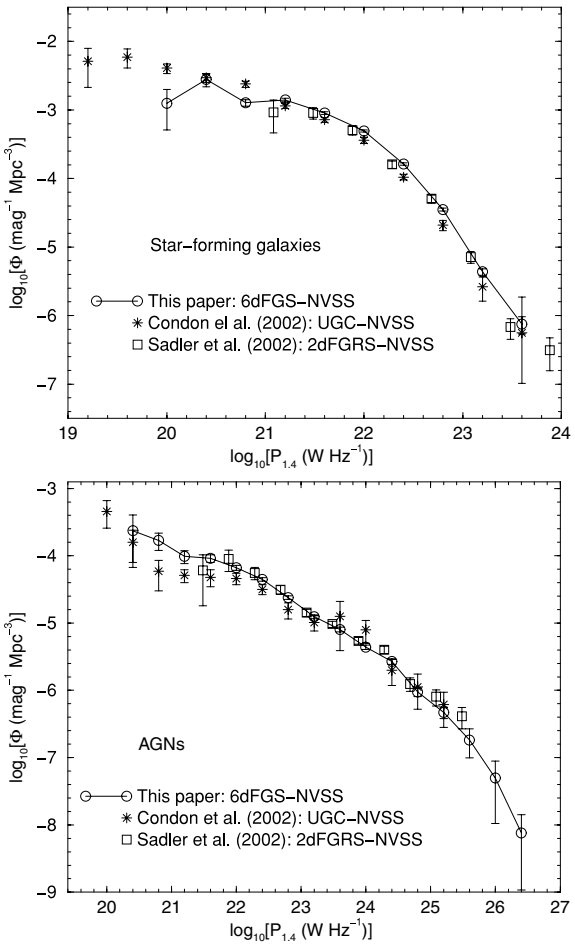

Figure 13. The local RLF at 1.4 GHz for SF galaxies (top) and radio-loud AGNs (bottom), comparing results from three different samples. The UGC–NVSS luminosity functions of Condon et al. (2002) are shown as stars. The 2dFGRS–NVSS luminosity functions of Sadler et al. (2002) are shown as boxes and have been modified from $H_0 = 50\,\mathrm{km\,s^{-1}\,Mpc^{-1}}$ to $H_0 = 70\,\mathrm{km\,s^{-1}\,Mpc^{-1}}$ by the scaling factor $P_{1.4} \propto H_0^{-2}$ and $\Phi \propto H_0^3$. The 6dFGS–NVSS luminosity functions are shown as circles with a line linking the points to highlight their position.

to the large-scale radio emission seen in many nearby radio sources. We therefore believe that Magliocchetti et al. (2002) have underestimated the total flux density of many of the radio sources in the 2dFGRS–FIRST sample. The 6dFGS–NVSS sample presented here samples a larger volume of space than the other radio source samples and probes look-back times intermediate between the nearby UGC–NVSS sample and the more distant 2dFGRS–NVSS one. These three luminosity functions are all drawn from the same radio source catalogue and differ only in the optical/NIR samples from which they are selected. The agreement between them is striking.

5.5.1 Star-forming galaxies

The 6dFGS–NVSS luminosity function of SF galaxies in the upper panel of Fig. 13 agrees with the other two over the range $10^{20.5} < P_{1.4} < 10^{22}\,\mathrm{W\,Hz^{-1}}$. The fall-off at the $P_{1.4} = 10^{20}\,\mathrm{W\,Hz^{-1}}$ point is caused by the small numbers of low luminosity SF galaxies in the 6dFGS sample volume and can also be seen at the lowest radio powers in the luminosity function of 2dFGRS–NVSS galaxies. The UGC–NVSS luminosity function extends about an order of magnitude deeper in radio power for SF galaxies, reflecting the larger number of low-luminosity radio sources detected in a flux density limited sample covering a larger solid angle. The 6dFGS–NVSS luminosity function of SF galaxies does not fall as steeply as the other two at the highest radio powers ($P_{1.4} > 10^{22.5}\,\mathrm{W\,Hz^{-1}}$). We believe this is caused by the NIR selection of the 6dFGS–NVSS sample.

5.5.2 Radio-loud AGNs

The radio-loud AGN luminosity function of 6dFGS–NVSS galaxies agrees well with the UGC–NVSS radio-loud AGN luminosity function. The UGC–NVSS radio-loud AGN sample consists of only 294 objects and is therefore not as well constrained. Most of the large error bars in the UGC–NVSS radio-loud AGN luminosity function overlap with the 6dFGS–NVSS points. A power-law fit to the 6dFGS–NVSS luminosity function below $\log_{10}[P_{1.4}\ (\mathrm{W\,Hz^{-1}})] = 25.0$ is

$$\log_{10}[\Phi(P_{1.4})] = (-0.61 \pm 0.02)\log[P_{1.4}] + (9.33 \pm 0.53) \quad (7)$$

and to the 2dFGRS–NVSS luminosity function is

$$\log_{10}[\Phi(P_{1.4})] = (-0.62 \pm 0.03)\log[P_{1.4}] + (9.42 \pm 0.70). \quad (8)$$

The 2dFGRS–NVSS luminosity function has the same power-law form as the 6dFGS–NVSS luminosity function over nearly four orders of magnitude. The present data are insufficient to measure any possible evolution over the narrow redshift range of $\tilde{z} = 0.07$ to $\tilde{z} = 0.14$ between the two samples.

6 THE STAR FORMATION DENSITY AT THE PRESENT EPOCH

Radio emission from SF galaxies is the product of massive ($M \geqslant 8\,\mathrm{M_\odot}$) stars which have short lifetimes ($\tau \sim 10^7$ yr). Roughly 90 per cent of this radio emission comes from non-thermal synchrotron electrons, which have been accelerated in the remnants of Type II supernovae, and the remainder comes from ionized hydrogen gas in H II regions heated by the most massive stars. This means that the radio luminosity of SF galaxies is roughly proportional to the rate of recent ($\tau \sim 10^8$ yr) star formation (Condon 1992). It is therefore possible to use the SF galaxies in this sample to estimate the present epoch star formation density of the universe for galaxies with $K \leqslant 12.75$ mag, which is the zero-point of the Madau diagram (Madau et al. 1996). Estimates of the local star formation density made from radio surveys are particularly robust as they are free from the effects of dust extinction. Effects of extinction are minimized in the 6dFGS–NVSS sample, as the radio selection is made from a NIR galaxy sample.

6.1 Calculating the star formation density

It is possible to estimate the local star formation density as a function of star formation rate directly from the RLF using a method described by Cram (1998) and Haarsma et al. (2000). Assuming a typical Salpeter-like initial mass function (IMF) of the form

$$\Psi(M) \propto M^{-2.35} \quad (9)$$

between 0.1 and 100 $\mathrm{M_\odot}$, the star formation rate of stars more massive than 0.1 $\mathrm{M_\odot}$ (in $\mathrm{M_\odot\,yr^{-1}}$) can be calculated from the 1.4 GHz radio power by the relation

$$\mathrm{SFR(P_{1.4})} = \frac{P_{1.4}}{8.85 \times 10^{20}} \quad (10)$$

(Sullivan et al. 2001). The star formation density can then be determined as a function of star formation rate by multiplying the star formation rate by the space density of radio sources, or simply

$$\rho_{SF}(\mathrm{SFR}) = \mathrm{SFR}(P_{1.4}) \times \Phi(P_{1.4}) \quad (11)$$

in $\mathrm{M_\odot\,yr^{-1}\,mag^{-1}\,Mpc^{-3}}$. Fig. 14 shows equation (11) for the luminosity function of 6dFGS–NVSS SF galaxies. SF galaxies in the 6dFGS–NVSS sample trace star formation rates between 0.1 and $500\,\mathrm{M_\odot\,yr^{-1}}$, though the major contribution to the local star formation density comes from galaxies with star formation rates around $10\,\mathrm{M_\odot\,yr^{-1}}$ as has been seen in other determinations of the star formation density of the local universe (e.g. radio; Sadler et al. 2002 and Hα; Gallego et al. 1995).

Integrating underneath the curve in Fig. 14 gives an estimate of the global star formation density at the present epoch (ρ_{SF}). The vast majority of radio sources in this sample contribute to the integral near its maximum at $10\,\mathrm{M_\odot\,yr^{-1}}$; the less certain points below this maximum make little contribution to the integral. This implies that the global star formation density will be accurately constrained by

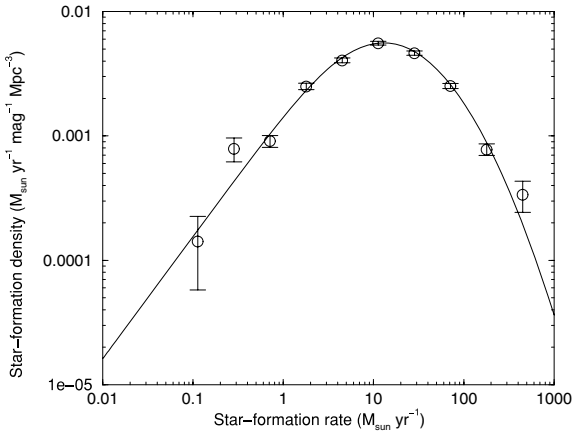

Figure 14. The variation in star formation density (ρ_{SF}(SFR)) with star formation rate for galaxies with star formation rates between 0.1 and $100\,\mathrm{M_\odot\,yr^{-1}}$ as derived from equation (11). Values of Φ have been taken from Table 5 for SF galaxies with the errors scaled appropriately. The curve is derived from the fit of equation (5) to the luminosity function of SF galaxies.

the data. Rather than compute the global star formation density from the binned data in Fig. 14 it is preferable to compute $\rho_{\rm SF}$ directly from a sum over each sample galaxy. This is done by computing the local power density function $[u(P_{1.4})]$,

The total radio power produced per unit volume of space $U_{\rm SF}$ (in units of W Hz^{-1} Mpc^{-3}) is just the integral over all radio powers of the power density function

$$U_{\rm SF} = \int_0^\infty u(P_{1.4})\,{\rm d}P_{1.4}, \tag{12}$$

which can be calculated directly as the sum over all galaxies of $P_{1.4}/V_{\rm max}$. $U_{\rm SF}$ is directly proportional to the star formation rate density $\rho_{\rm SF}$ and is computed using the relation

$$\rho_{\rm SF} = 1.13 \times 10^{-21} U_{\rm SF} \tag{13}$$

the factor 1.13×10^{-21} comes from the conversion between star formation rate and radio power in equation (10).

6.2 Results

The global power density of star formation at the present epoch implied by the 6dFGS–NVSS sample is $U_{\rm SF} = (1.91 \pm 0.09) \times 10^{19}$ W Hz^{-1} Mpc^{-3}. This translates to a global star formation density

$$\rho_{\rm SF} = (0.022 \pm 0.001)\ {\rm M}_\odot\ {\rm yr}^{-1}\,{\rm Mpc}^{-3}. \tag{14}$$

The uncertainty in $\rho_{\rm SF}$ quoted here is purely statistical and takes no account of the errors arising from the conversion from $P_{1.4}$ to star formation rate in equation (10). Errors in this conversion come primarily from predicting the star formation rate from the Type II SNe rate, which contributes 90 per cent of the radio power at 1.4 GHz (Sullivan et al. 2001), from models of the total radio spectral energy per Type II supernova and from the assumption of a Salpeter-like IMF in equation (9).

Values for $\rho_{\rm SF}$ measured from the UGC–NVSS and 2dFGRS–NVSS samples are shown in Table 1. The value of $\rho_{\rm SF}$ for 6dFGS–NVSS galaxies is intermediate between values those for the other samples. Condon et al. (2002) derived $\rho_{\rm SF} = 0.018 \pm 0.001\,{\rm M}_\odot$ yr^{-1} Mpc^{-3} for the UGC–NVSS sample of 1672 SF galaxies and Sadler et al. (2002) derived $\rho_{\rm SF} = 0.031 \pm 0.006$ M$_\odot$ yr^{-1} Mpc^{-3} (converted to $H_0 = 70$ km s^{-1} Mpc^{-1}) for 242 SF galaxies from the 2dFGRS–NVSS sample. Differences in the measured values of $\rho_{\rm SF}$ between the three radio samples are likely to be caused by their different optical/NIR magnitude limits. Fainter and hence less massive galaxies can make a significant contribution to the local star formation density (Brinchmann et al. 2004). For example, from fig. 15 of Brinchmann et al. (2004) we estimate that the $K = 12.75$ magnitude limit of the 6dFGS–NVSS means the sample misses at least $\sim$0.004 M$_\odot$ yr^{-1} Mpc^{-3} of the local star formation density measured from Hα. The 2dFGRS–NVSS sample on the other hand has an optical limit about 2 mag fainter than the 6dFGS–NVSS sample and misses only a negligible amount of local star formation. Further differences between the three samples are probably the result of evolution in the star formation density over the narrow redshift range.

Uncertainties in the relationship between monochromatic radio power and star formation rate do not affect models describing the relationship between star formation rate and luminosities at shorter wavelengths. However, dust extinction within the H II regions where star formation occurs contributes increasingly to the model uncertainties at these shorter wavelengths. The value of $\rho_{\rm SF}$ measured here has been compared with other recent determinations measured from a broad range of wavelengths by Hopkins & Beacom (2006). The interested reader is referred to this paper for more information. The general agreement (usually to within a factor of 2) between values of $\rho_{\rm SF}$ at different wavebands is reassuring.

7 BIVARIATE RADIO–NIR LUMINOSITY FUNCTIONS

The local RLF of radio-loud AGNs presented in Section 5 contains large numbers of galaxies in most bins of radio power, which enables us to split it into statistically significant subclasses. In particular, the local RLFs can be broken into bins of absolute K-band magnitude (M_K) to examine the radio properties of galaxies of different NIR luminosities. The NIR selection of the 6dFGS–NVSS sample is of particular importance here, as the K-band galaxy luminosity is an extinction-free estimator of the mass of the old stellar population in galaxies. The vast majority of radio-loud AGNs reside in early-type galaxies whose absolute K-band magnitude gives an indication of their bulge mass which in turn is correlated with the black hole mass (e.g. Marconi & Hunt 2003). It is therefore possible to examine how the properties of radio-loud AGNs may vary with black hole mass.

One of the first bivariate radio-optical luminosity functions was determined by Auriemma et al. (1977) from a sample of radio detections of bright elliptical galaxies. They showed that the probability of an elliptical galaxy to host a radio-loud AGN increases strongly as a function of optical luminosity. Further studies using larger samples of elliptical galaxies were carried out by Sadler, Jenkins & Kotanyi (1989) and Ledlow & Owen (1996) who verified the result of Auriemma et al. (1977) and found that the break in RLF scaled strongly with host galaxy luminosity. More recently Best et al. (2005a) used the SDSS–NVSS/FIRST sample of 2215 galaxies to calculate accurate bivariate radio luminosity-mass functions, from both host-galaxy mass and black hole mass. They found that the *fraction* of galaxies hosting a radio-loud AGN increases strongly as a function of both galaxy and black hole masses. Best et al. (2005a) also argued that there was no evidence for any dependence of the break luminosity on black hole mass.

Here, we measure the bivariate radio–NIR luminosity function for the first time which we can compare with bivariate radio-optical luminosity functions. The 6dFGS–NVSS bivariate luminosity function is calculated from accurate *observed* quantities measured from homogeneous all-sky surveys. We therefore avoid any errors which may arise from calculating the bivariate luminosity function from *derived* quantities. For example, the large observed scatter in the $M_{\rm bh} - \sigma$ relation of 0.3 dex (Tremaine et al. 2002) is a significant source of error in the bivariate radio luminosity versus black hole mass function measured by Best et al. (2005a).

7.1 Calculating the bivariate luminosity function

When separating the RLF into M_K bins it is preferable to define a normalized, or fractional luminosity function

$$F_K(P_{1.4}) = \frac{\phi_K(P_{1.4})}{\rho_K} \tag{15}$$

which is the RLF of galaxies in M_K bin $M_K \pm \Delta M_K$($\phi_K(P_{1.4})$ in Mpc^{-3}) divided by the volume density (ρ_K in Mpc^{-3}) of *all* galaxies with absolute magnitude in the M_K-magnitude bin $M_K \pm \Delta M_K$. The RLF in each K-band magnitude bin $\phi_K(P_{1.4})$ is calculated using the $1/V_{\rm max}$ method (Schmidt 1968) in 1-mag radio luminosity bins of width 0.4 in log ($P_{1.4}$). This gives $\phi_K(P_{1.4})$ in units of mag^{-1} Mpc^{-3}. With this definition $F_K(P_{1.4})\ {\rm d}P_{1.4}$ represents the fraction of all

Table 6. The bivariate radio-*K*-band luminosity function of radio-loud AGNs.

$\log_{10} P_{1.4}$	$-23 > M_K \geqslant -24$ ($\rho_K = 1.88 \times 10^{-3}$)		$-24 > M_K \geqslant -25$ ($\rho_K = 1.14 \times 10^{-3}$)		$-25 > M_K \geqslant -26$ ($\rho_K = 2.10 \times 10^{-4}$)		$-26 > M_K \geqslant -27$ ($\rho_K = 9.92 \times 10^{-6}$)	
($\mathrm{W\,Hz^{-1}}$)	N	$\log_{10}[F_K(P_{1.4})]$	N	$\log_{10}[F_K(P_{1.4})]$	N	$\log_{10}[F_K(P_{1.4})]$	N	$\log_{10}[F_K(P_{1.4})]$
20.4	1	$-1.49^{+0.30}_{-1.00}$			1	$-1.05^{+0.30}_{-1.00}$		
20.8	3	$-1.70^{+0.20}_{-0.38}$	7	$-1.12^{+0.14}_{-0.21}$	1	$-1.34^{+0.30}_{-1.00}$		
21.2	7	$-1.80^{+0.14}_{-0.22}$	10	$-1.45^{+0.12}_{-0.17}$	4	$-1.15^{+0.18}_{-0.31}$		
21.6	16	$-1.93^{+0.10}_{-0.14}$	38	$-1.33^{+0.07}_{-0.08}$	8	$-1.28^{+0.14}_{-0.22}$		
22.0	31	$-2.11^{+0.07}_{-0.09}$	76	$-1.62^{+0.05}_{-0.06}$	49	$-1.05^{+0.06}_{-0.07}$		
22.4	19	$-2.59^{+0.09}_{-0.12}$	189	$-1.74^{+0.03}_{-0.03}$	161	$-1.11^{+0.04}_{-0.04}$	5	$-1.20^{+0.17}_{-0.29}$
22.8	8	$-2.90^{+0.14}_{-0.20}$	148	$-2.08^{+0.04}_{-0.04}$	380	$-1.25^{+0.02}_{-0.02}$	14	$-1.49^{+0.11}_{-0.15}$
23.2	4	$-3.35^{+0.18}_{-0.31}$	57	$-2.52^{+0.06}_{-0.07}$	359	$-1.46^{+0.02}_{-0.03}$	105	$-1.03^{+0.04}_{-0.05}$
23.6	2	$-3.71^{+0.23}_{-0.54}$	44	$-2.61^{+0.07}_{-0.08}$	209	$-1.69^{+0.03}_{-0.03}$	93	$-1.22^{+0.04}_{-0.05}$
24.0			14	$-3.21^{+0.10}_{-0.14}$	167	$-1.82^{+0.03}_{-0.04}$	77	$-1.31^{+0.05}_{-0.06}$
24.4			6	$-3.51^{+0.15}_{-0.23}$	99	$-2.06^{+0.04}_{-0.05}$	74	$-1.31^{+0.05}_{-0.06}$
24.8			3	$-3.89^{+0.20}_{-0.38}$	33	$-2.60^{+0.07}_{-0.09}$	42	$-1.57^{+0.07}_{-0.08}$
25.2			1	$-4.42^{+0.30}_{-1.00}$	10	$-3.00^{+0.12}_{-0.17}$	36	$-1.67^{+0.07}_{-0.08}$
25.6			1	$-4.17^{+0.30}_{-1.00}$	4	$-3.55^{+0.18}_{-0.31}$	10	$-2.33^{+0.12}_{-0.18}$
26.0					2	$-3.64^{+0.26}_{-0.73}$		
Total	91		594		1487		456	

galaxies in the absolute NIR magnitude bin $M_K \pm \Delta M_K$ that have radio power between $P_{1.4}$ and $P_{1.4} + \mathrm{d}P_{1.4}$.

To determine ρ_K, the volume density of galaxies with absolute NIR magnitude M_K, it is convenient to use the *K*-band galaxy luminosity function Φ_K. It is important that the *K*-band luminosity function used be subject to the same selection criteria as the radio sample, so as not to introduce biases from cosmic variance into the data. We use the $1/V_{\mathrm{max}}$ determination of the 6dFGS *K*-band luminosity function described by Jones et al. (2006). Its error bars are much smaller than those in the 6dFGS–NVSS luminosity function and are therefore ignored when calculating $F_K(P_{1.4})$.

7.2 The bivariate radio–NIR luminosity function of radio-loud AGNs

Table 6 lists and Fig. 15 shows $F_K(P_{1.4})$ for radio-loud AGNs in four bins of M_K. Below $F_K(P_{1.4}) = 0.1$ the broad break between $P_{1.4} = 10^{24}$ and 10^{25} $\mathrm{W\,Hz^{-1}}$ seen in the RLF in Fig. 12 can be seen in the brightest M_K bins ($M_K = -25.5, -26.5$). In the faintest two bins ($M_K = -23.5, -24.5$), the data do not extend to high enough radio powers to detect a break. In the brightest bins of M_K the fractional luminosity function turns over below the radio power at which $F_K(P_{1.4}) = 0.1$. It is probable that this turnover is caused by the normalization of the fractional luminosity function; a larger fraction of radio sources cannot be measured at a given M_K because nearly all available galaxies are detected. The turnover occurs at fainter radio powers in less luminous galaxies, this is probably because both less luminous galaxies and less powerful radio sources have higher space density.

There is a clear decrease with radio power in the fraction of galaxies which are radio-loud AGNs for all M_K, reflecting the decrease in space density of radio-loud AGNs with increasing radio power. For a given radio power, there is a strong increase in the fraction of galaxies which are radio-loud AGNs with brightening M_K. More luminous galaxies are therefore more likely to host a radio-loud AGN as has been seen in previous determinations of the fractional radio-optical luminosity function of elliptical galaxies. To properly quantify this effect we determine the fractional luminosity function in its integral form.

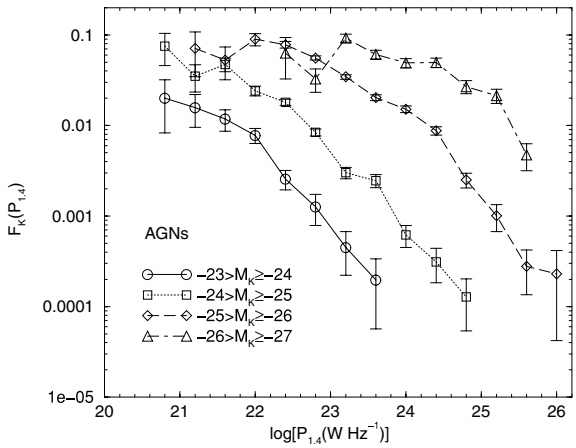

Figure 15. The fractional luminosity function of radio-loud AGNs calculated using the procedure described in Section 7.1 of the text. $F_K(P_{1.4})$ is calculated in four bins of absolute *K* magnitude (M_K) as labelled in the figure. The two M_K bins centred at -25.5 and -26.5 are brighter than $M_K^{\star} = -24.6$.

7.3 The integral bivariate radio–NIR luminosity function of radio-loud AGNs

The integral form of the fractional luminosity function at a particular radio power ($F_K(>P_{1.4})$) is calculated in each M_K bin from the sum of $F_K(P_{1.4})$ between the largest bin of radio power ($P_{1.4}^{\mathrm{max}}$) to $P_{1.4}$. It measures the fraction of all galaxies which are radio sources with powers greater than $P_{1.4}$ in each M_K bin. It is not straightforward to calculate the error at each point of $F_K(>P_{1.4})$ because the points are

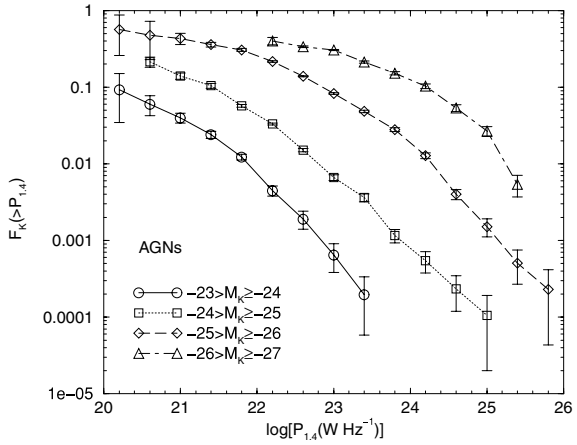

Figure 16. The fractional luminosity function of radio-loud AGNs in integral form. $F_K(>P_{1.4})$ denotes the fraction of all galaxies which host a radio-loud AGN with radio power greater than $P_{1.4}$. Errors have been calculated using the bootstrap method with 10^6 iterations.

not independent. For this reason we calculated errors in each radio power bin of $F_K(>P_{1.4})$ using bootstrap analysis with 10^6 iterations.

Fig. 16 shows the fractional luminosity function of radio-loud AGNs in integral form in four bins of M_K, with bootstrap errors. With the available data, radio powers at which 40–50 per cent of galaxies are detected as radio-loud AGNs are reached at the brightest M_K bins. The function has approximately the same shape for all bins of M_K though this breaks down above $F_K(>P_{1.4}) = 0.3$ which is caused by the turnover in $F_K(P_{1.4})$ discussed in Section 7.2. Best et al. (2005a) also found a ceiling in the bivariate radio luminosity-mass function of SDSS–NVSS/FIRST galaxies at the 30 per cent level. We determine the dependence of $f_{\rm radio-loud}$ (the fraction of all galaxies that are radio-loud) on L_K by scaling $F_K(>P_{1.4})$ to remove the dependence on M_K. The best-fitting scaling factor for $F_K(>P_{1.4}) < 0.3$ is $f_{\rm radio-loud} \propto L_K^{2.1}$; clearly, the probability of a galaxy to host radio-loud AGNs is a strong function of its *K*-band luminosity.

Given that the majority (>70 per cent) of the radio-loud AGNs in the 6dFGS–NVSS sample reside in early-type galaxies, their total *K*-band luminosity should be close to or equal to their NIR bulge luminosity ($L_{K,\rm bul}$). Assuming this, the *K*-band luminosities of these radio-loud AGNs are indicative of the black hole mass of the galaxy via the $M_{\rm BH}$ –$L_{K,\rm bul}$ correlation (Marconi & Hunt 2003). The precise scaling is uncertain though, as it is unclear at this stage of the precise contribution from disks to the *K*-band luminosity of the radio-loud AGNs in our sample. An accurate derivation of the *K*-band bulge luminosity of all 6dFGS galaxies is beyond the scope of this paper. Accurate velocity dispersions will be measured from spectra of the 15 000 brightest elliptical galaxies in the 6dFGS(Jones et al. 2004). We expect to detect about 30 per cent of these in the NVSS (see Fig. 16). A full analysis of these galaxies will be the subject of a future paper.

8 CONCLUSION

In this paper we have derived a catalogue of 7824 radio sources from the NVSS catalogue which have been observed in the 6dFGS DR2 *K*-selected primary sample. The main results of this paper are as follows.

(i) The median redshift of all radio sources in the sample is $\tilde{z} = 0.046$, which is similar to that of the 47 317 *K*-band selected galaxies from which the radio sources were selected. 60 per cent of 6dFGS–NVSS primary targets are spectroscopically identified as SF galaxies which form a much more nearby population ($\tilde{z} = 0.035$) and 40 per cent of 6dFGS–NVSS primary targets are identified as radio-loud AGNs which form a more distant population ($\tilde{z} = 0.073$).

(ii) SF galaxies and radio-loud AGNs have quite distinct distributions in the plane of radio power versus absolute *K* magnitude. SF galaxies tend to have radio powers $P_{1.4} < 10^{23}$ W Hz^{-1}, though they have a wide range of absolute *K* magnitudes. The radio-loud AGNs span a wide range in radio power but are almost all found in the most luminous NIR galaxies with $M_K > M_K^\star$.

(iii) 2690 SF galaxies and 208 radio-loud AGNs were detected at 60 μm in the *IRAS*–FSC. All of the SF galaxies with *IRAS*–FSC detections in the 6dFGS–NVSS sample are found to lie on the radio–FIR correlation, with average FIR–radio flux ratio parameter $\langle q_{\rm SF} \rangle = 2.3$ with rms scatter $\sigma_{\rm SF} = 0.18$, in close agreement with the results of other recent radio–FIR surveys (UGC–NVSS; Condon et al. 2002). Many of the 208 radio-loud AGNs with *IRAS*–FSC 60 μm detections also lie on the radio–FIR correlation. However, these tend to have hotter *IRAS* 60–25 μm colours. The combination of the radio–FIR correlation and the 60–25 μm colour as a means of AGN/SF classification for radio sources agrees with spectroscopic classification for more than 90 per cent of all galaxies, which is reassuring considering the differences in these classification techniques.

(iv) We have measured accurate and homogeneous local RLFs at 1.4 GHz of SF galaxies and radio-loud AGNs. The luminosity functions presented here agree well with recent determinations of the local RLF derived from different optical samples (e.g. UGC–NVSS, Condon et al. 2002; 2dFGRS–NVSS, Sadler et al. 2002).

(v) The star formation density at the present epoch has been measured from the 6dFGS–NVSS sample and was found to be $\rho_{SF} = (0.022 \pm 0.001)\,{\rm M}_\odot\,{\rm yr}^{-1}\,{\rm Mpc}^{-3}$, in agreement with previously derived values at radio and other wavelengths.

(vi) We have split the RLF of radio-loud AGNs into four bins of M_K and compared with the *K*-band luminosity function of all 6dFGS galaxies to calculate a fractional luminosity function $F_K(P_{1.4})$. We find that $F_K(P_{1.4})$ for radio-loud AGNs increases strongly as a function of NIR luminosity, which in turn is indicative of an increasing probability for a galaxy to host a radio-loud AGN with increasing black hole mass.

ACKNOWLEDGMENTS

We would like to thank the Anglo-Australian Observatory staff at the UK Schmidt Telescope and the entire 6dFGS team for ensuring the success of the 6dFGS. We thank D. Heath Jones for providing early versions of the 6dFGS *K*-band galaxy luminosity function for analysis. We thank the referee for carefully reading the paper and useful comments which improved the final version. This research uses the NVSS radio survey, carried out using the National Radio Astronomy Observatory (NRAO) Very Large Array. The NRAO is a facility of the National Science Foundation operated under cooperative agreement by Associated Universities, Inc. TM acknowledges the financial support of an Australian Postgraduate Award. EMS acknowledges support from the Australian Research Council through the award of an ARC Australian Professorial Fellowship.

REFERENCES

Auriemma C., Perola G. C., Ekers R. D., Fanti R., Lari C., Jaffe W. J., Ulrich M. H., 1977, A&A, 57, 41

Becker R. H., White R. L., Helfand D. J., 1995, ApJ, 450, 559

Best P. N., Kauffmann G., Heckman T. M., Brinchmann J., Charlot S., Ivezić Ž., White S. D. M., 2005a, MNRAS, 362, 25
Best P. N., Kauffmann G., Heckman T. M., Ivezić Ž., 2005b, MNRAS, 362, 9
Best P. N., Kaiser C. R., Heckman T. M., Kauffmann G., 2006, MNRAS, 368, L67
Bock D. C.-J., Large M. I., Sadler E. M., 1999, ApJ, 117, 1578
Brinchmann J., Charlot S., White S. D. M., Tremonti C., Kauffmann G., Heckman T., Brinkmann J., 2004, MNRAS, 351, 1151
Brown M. J. I., Webster R. L., Boyle B. J., 2001, AJ, 121, 2381
Bruzual A. G., Charlot S., 1993, ApJ, 405, 538
Campbell L., Saunders W., Colless M., 2004, MNRAS, 350, 1467
Cole S. et al., 2001, MNRAS, 326, 255
Colless M. et al., 2001, MNRAS, 328, 1039
Condon J. J., 1989, ApJ, 338, 13
Condon J. J., 1992, ARA&A, 30, 575
Condon J. J., Broderick J. J., 1988, AJ, 96, 30
Condon J. J., Anderson M. L., Helou G., 1991, ApJ, 376, 95
Condon J. J., Helou G., Sanders D. B., Soifer B. T., 1993, AJ, 105, 1730
Condon J. J., Cotton W. D., Greisen E. W., Yin Q. F., Perley R. A., Taylor G. B., Broderick J. J., 1998, AJ, 115, 1693
Condon J. J., Cotton W. D., Broderick J. J., 2002, AJ, 124, 675
Cowie L. L., Barger A. J., Fomalont E. B., Capak P., 2004, ApJ, 603, L69
Cram L. E., 1998, ApJ, 506, L85
de Grijp M. H. K., Keel W. C., Miley G. K., Goudfrooij P., Lub J., 1992, A&AS, 96, 389
Devereux N. A., Eales S. A., 1989, ApJ, 340, 708
Drake C. L., McGregor P. J., Dopita M. A., van Breugel W. J. M., 2003, AJ, 126, 2237
Dunlop J. S., Peacock J. A., 1990, MNRAS, 247, 19
Folkes S. O., 1999, MNRAS, 308, 459
Gallego J., Zamorano J., Aragon-Salamanca A., Rego M., 1995, ApJ, 455, L1
Glazebrook K., Peacock J. A., Miller L., Collins C. A., 1995, MNRAS, 275, 169
Griffith M. R., Wright A. E., 1993, AJ, 105, 1666
Haarsma D. B., Partridge R. B., Windhorst R. A., Richards E. A., 2000, ApJ, 544, 641
Hambly N. C. et al., 2001, MNRAS, 326, 1279
Helou G., Soifer B. T., Rowan-Robinson M., 1985, ApJ, 298, L7
Hopkins A. M., Beacom J. F., 2006, ApJ, 652, 142
Jackson C. A., Londish D. M., 2000, Publ. Astron. Soc. Aust., 17, 234
Jackson C. A., Wall J. V., 1999, MNRAS, 304, 160
Jarrett T. H., Chester T., Cutri R., Schneider S., Skrutskie M., Huchra J. P., 2000, AJ, 119, 2498
Jones D. H. et al., 2004, MNRAS, 355, 747
Jones D. H., Saunders W., Read M., Colless M., 2005, Publ. Astron. Soc. Aust., 22, 277
Jones D. H., Peterson B. A., Colless M., Saunders W., 2006, MNRAS, 369, 25
Kauffmann G. et al., 2003, MNRAS, 346, 1055
Laing R. A., Riley J. M., Longair M. S., 1983, MNRAS, 204, 151
Large M. I., Mills B. Y., Little A. G., Crawford D. F., Sutton J. M., 1981, MNRAS, 194, 693
Lawrence A., Walker D., Rowan-Robinson M., Leech K. J., Penston M. V., 1986, MNRAS, 219, 687
Ledlow M. J., Owen F. N., 1996, AJ, 112, 9
Madau P., Ferguson H. C., Dickinson M. E., Giavalisco M., Steidel C. C., Fruchter A., 1996, MNRAS, 283, 1388
Madgwick D. S. et al., 2002, MNRAS, 333, 133
Magliocchetti M. et al., 2002, MNRAS, 333, 100
Marconi A., Hunt L. K., 2003, ApJ, 589, L21
Mauch T., 2006, PhD thesis, Univ. Sydney
Mauch T., Murphy T., Buttery H. J., Curran J., Hunstead R. W., Piestrzynski B., Robertson J. G., Sadler E. M., 2003, MNRAS, 342, 1117
Moshir M. et al., 1993, VizieR Online Data Catalog, 2156
Nilson P., 1973, Uppsala General Catalogue of Galaxies. Acta Universitatis Upsaliensis. Nova Acta Regiae Societatis Scientiarum Upsaliensis – Uppsala Astronomiska Observatoriums Annaler. Astronomiska Observatorium, Uppsala
Nipoti C., Binney J., 2005, MNRAS, 361, 428
Norris R. P., Roy A. L., Allen D. A., Kesteven M. J., Troup E. R., Reynolds J. E., 1992, in ASP Conf. Ser. Vol. 31, Relationships Between Active Galactic Nuclei and Starburst Galaxies. Astron. Soc. Pac., San Francisco, p. 71
Peebles P. J. E., 1980, The Large-scale Structure of the Universe. Research supported by the National Science Foundation. Princeton Univ. Press, Princeton, NJ, p. 435
Rengelink R., 1998, PhD thesis, Leiden University
Sadler E. M., Jenkins C. R., Kotanyi C. G., 1989, MNRAS, 240, 591
Sadler E. M., McIntyre V. J., Jackson C. A., Cannon R. D., 1999, Publ. Astron. Soc. Aust., 16, 247
Sadler E. M. et al., 2002, MNRAS, 329, 227
Sadler E. M. et al. 2006, MNRAS, submitted (astro-ph/0612019)
Sanders D. B., 2004, Adv. Space Res., 34, 535
Sanders D. B., Mirabel I. F., 1996, ARA&A, 34, 749
Saripalli L., Hunstead R. W., Subrahmanyan R., Boyce E., 2005, AJ, 130, 896
Saunders W., Rowan-Robinson M., Lawrence A., Efstathiou G., Kaiser N., Ellis R. S., Frenk C. S., 1990, MNRAS, 242, 318
Schechter P., 1976, ApJ, 203, 297
Schmidt M., 1968, ApJ, 151, 393
Schoenmakers A. P., de Bruyn A. G., Röttgering H. J. A., van der Laan H., 2001, A&A, 374, 861
Soifer B. T., Boehmer L., Neugebauer G., Sanders D. B., 1989, AJ, 98, 766
Spergel D. N. et al., 2003, ApJS, 148, 175
Sullivan M., Mobasher B., Chan B., Cram L., Ellis R., Treyer M., Hopkins A., 2001, ApJ, 558, 72
Tremaine S. et al., 2002, ApJ, 574, 740
York D. G. et al., 2000, AJ, 120, 1579

SUPPLEMENTARY MATERIAL

The following supplementary material is available for this article online.

Table 3. The 6dFGS–NVSS data table.
This material is available as part of the online paper from: http://www.blackwell-synergy.com/doi/abs/10.1111/j.1365-2966.2006.11353.x (this link will take you to the article abstract).

Please note: Blackwell Publishing are not responsible for the content or functionality of any supplementary materials supplied by the authors. Any queries (other than missing material) should be directed to the corresponding author for the article.

This paper has been typeset from a TEX/LATEX file prepared by the author.